SF newsletter 337 #15-21

M. Momose (Ibaraki Univ.)

15, 16, 18 (複数スライドで紹介)

19 (一枚のスライドで内容を紹介)

その他(アブストラクトのみ)

15.

The Carina Nebula and Gum 31 molecular complex III: The distribution of the 1-3 GHz radio continuum across the whole nebula

David Rebolledo, Anne J. Green, Michael G. Burton, Shari L. Breen, Guido Garay We report the most detailed $1-3$ GHz radio continuum emission map of the nearest region of massive star formation, the Carina Nebula. As part of a large program with the Australia Telescope Compact Array, we have covered ~ 12 deg^2, achieving an angular resolution of ~ 16 arcsec, representing the largest and most complete map of the radio continuum to date. Our continuum map shows a spectacular and complex distribution of emission across the nebula, with multiple structures such as filaments, shells, and fronts across a wide range of size scales. The ionization fronts have advanced far into the southern and northern region of the Galactic Plane, as fronts are clearly detected at distances ~ 80 pc from the stellar clusters in the center. We estimated an ionization photon luminosity $Q_{\rm H} = (7.8 \pm 0.8) \times 10^{50}$ s^{-1} which corresponds to $\sim 85\%$ of the total value obtained from stellar population studies. Thus, approximately 15% of the ionizing flux has escaped from the nebula into the diffuse Galactic Interstellar Medium. Comparison between radio continuum and the hydrogen atomic and molecular gas maps offers a clear view of the bipolar outflow driven by the energy released by the massive stellar clusters that also affects the fraction of molecular gas across the nebula. Comparison between 8μm and 70μm emission maps and the radio continuum reveals how the hot gas permeates through the molecular cloud, shapes the material into features such as pillars, small shells and arc-like structures, and ultimately, escapes.

- **Carina Nebulaの1-3GHz連続波をATCAを使ってかつてない広さ(12deg2)と完全さで16asecでマップ**
- **目を見張るイメージ取得**
  - **様々なスケールでのフィラメント・シェル・Fronts**
  - **電離フロントは銀画面から遠く離れたところ，星団中心から80pcにまで到達**
- **電離光子のLuminosity Q_H= (7.8±0.8) × $10^{50}$$s^{-1}$，星団からの電離光子の85%**
- **H原子との比較：アウトフロー構造の確認．そのほか，8umや70umとの比較も**

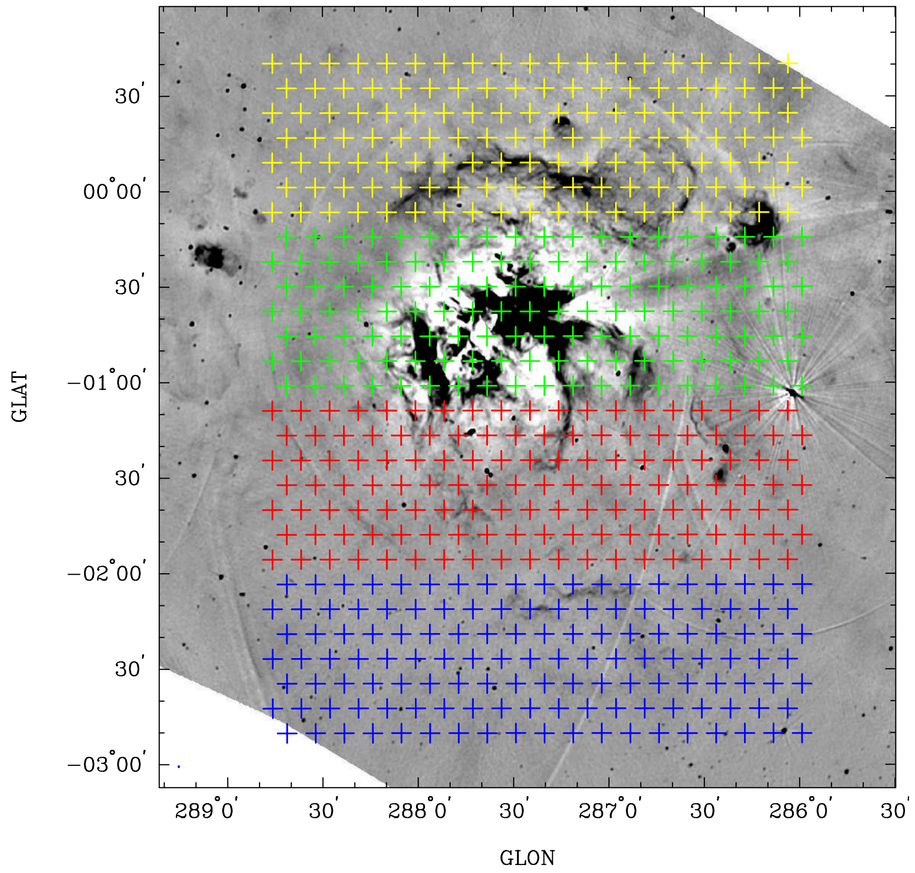

FIG. 1.— Mosaic pattern of our ATCA observations overlaid in a map of the 0.835 GHz continuum emission in the CNC-Gum 31 complex obtained with the Molonglo Observatory Synthesis Telescope (Green et al. 2014). In total, 532 pointings were observed, divided into 4 independent mosaics of 133 pointings each (illustrated with a different color). Each mosaic was observed using 11 array configurations to maximize $u-v$ coverage. Thus, our observing campaign completed 44 sessions with the ATCA. Each array configuration observation was individually calibrated before combination for final imaging.

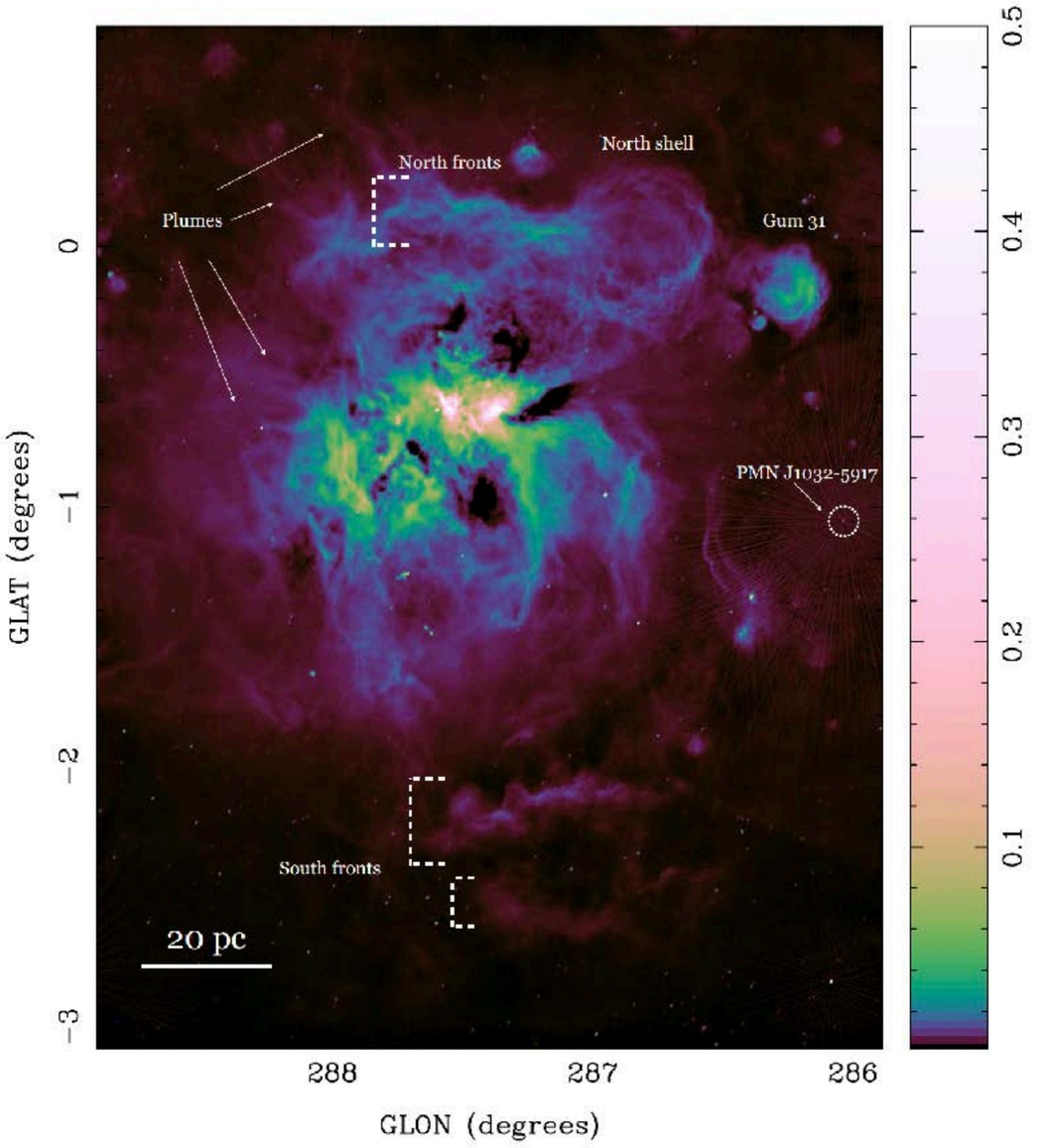

FIG. 4.— ATCA 1–3 GHz continuum image of the CNC-Gum31 complex. The image size is 3×4 deg^2, which was obtained with 532 pointing grid observations. Color bar is in Jy/beam. Our map provides an unprecedented high resolution and high fidelity radio continuum image of the Carina Nebula and surrounding regions. The spectacular and complex structure of the emission is revealed, with features similar to shells, filaments and ionization fronts. A large population of compact sources are also clearly detected across the surveyed area, the majority of which are extragalactic radio sources. Dashed white circle shows the position of the strong radio source PMN J1032-5917, which was subtracted from the uv-data.

中心部分の拡大図

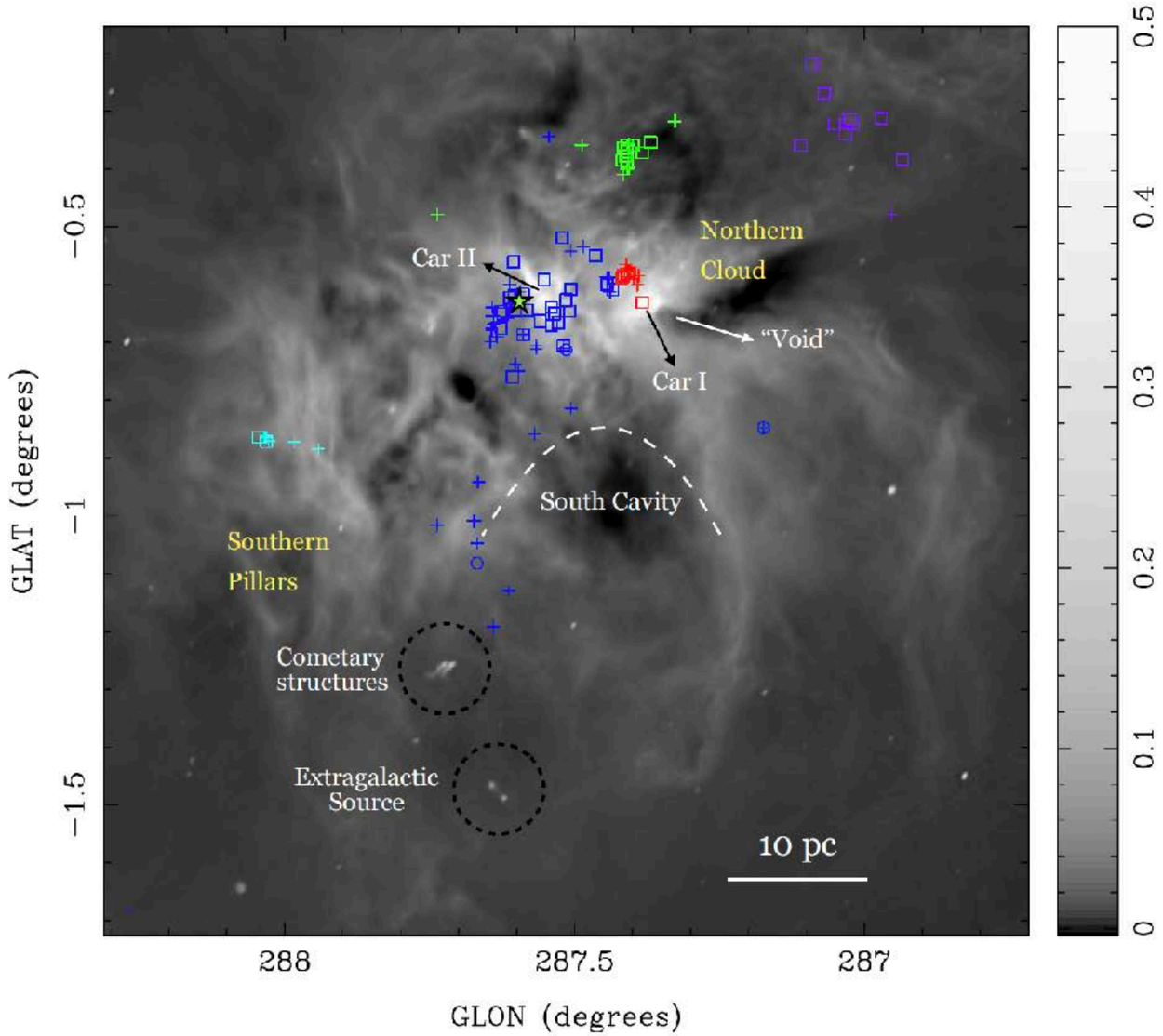

FIG. 5.— View of the radio continuum emission at 1−3 GHz in the central region of the CNC. Symbols show the position of the massive stars, with different colors illustrating different star clusters. Crosses show O stars, squares show B stars, and open circles show Wolf Rayet stars. Blue symbols show Trumpler 16 and Collinder 228 stellar clusters, red symbols show Trumpler 14, green show Trumpler 15, violet show Bochum 10 and cyan show Bochum 11 cluster as listed in Smith (2006). Black arrows show the position of the the two H II regions analyzed by Brooks et al. (2001), Car I and Car II. White arrow shows the "void" region where radio continuum emission seems to be absent. The curved white dashed line delineates the southern cavity discussed in the text. The black dashed circles shows the cometary objects and the extragalactic source discussed in Section 4.2

HIとの比較

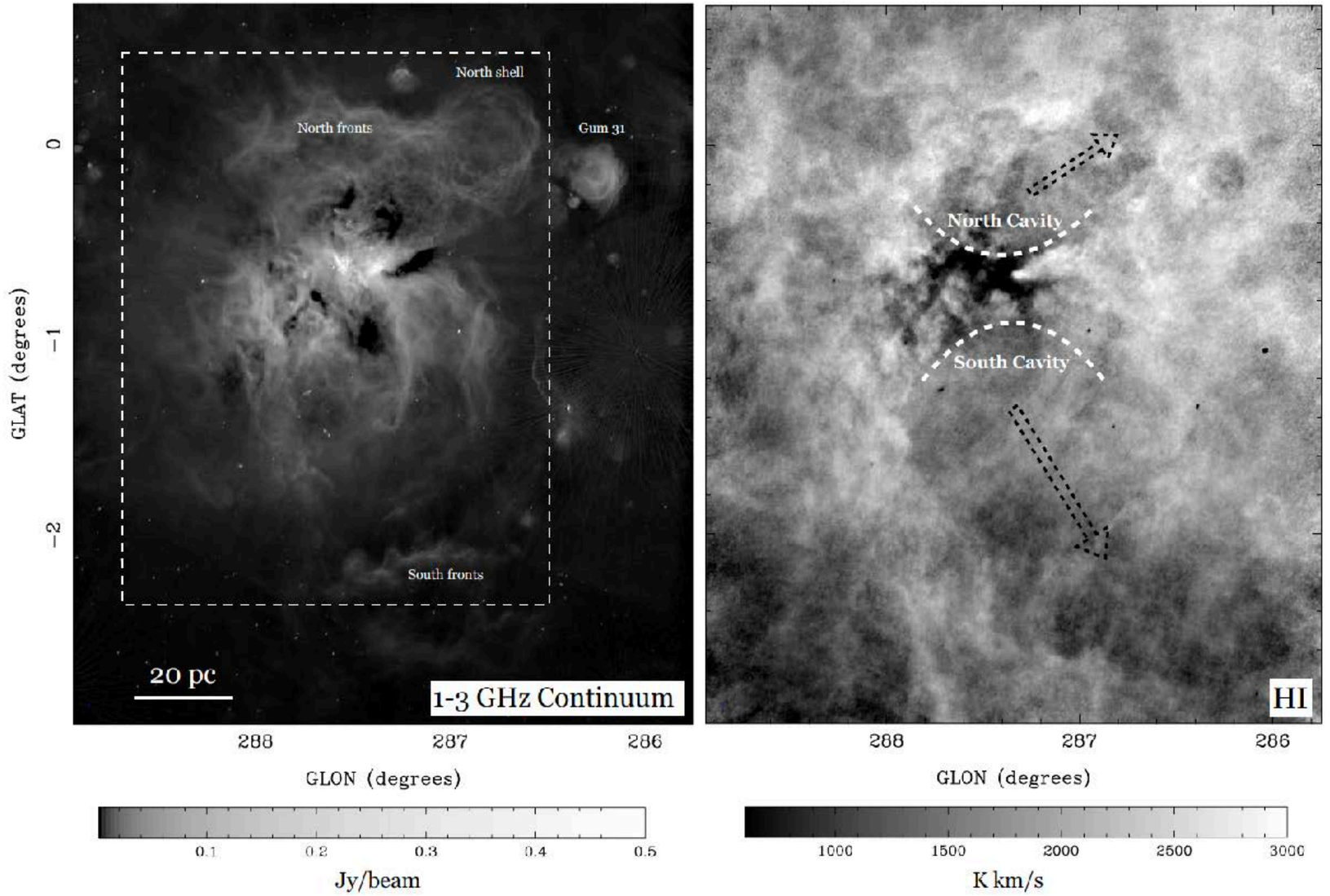

FIG. 6.— Two products of our ATCA Large Program observing campaign in the CNC-Gum 31 region, the 1 – 3 GHz radio continuum image (left) and the H I integrated intensity published in Paper II (right). The H I map was generated by integrating from −45 km s^{-1} to 0 km s^{-1}, the velocity range associated with the Carina region (Paper I). The white dashed-lined rectangle in the left panel shows the region used to estimate the total radio flux and hence derived the ionizing photon luminosity of Q_H. The curved white dashed lines in the H I integrated intensity map delineate the south and north cavities discussed in the text. The bipolar outflow generated by the massive stellar clusters located at the center of the Nebula is clearly detected in the H I map, and they are shown by the open black arrows. These two images can be compared to further investigate in detail the impact of the stellar feedback in the gas across the Nebula.

COとの比較

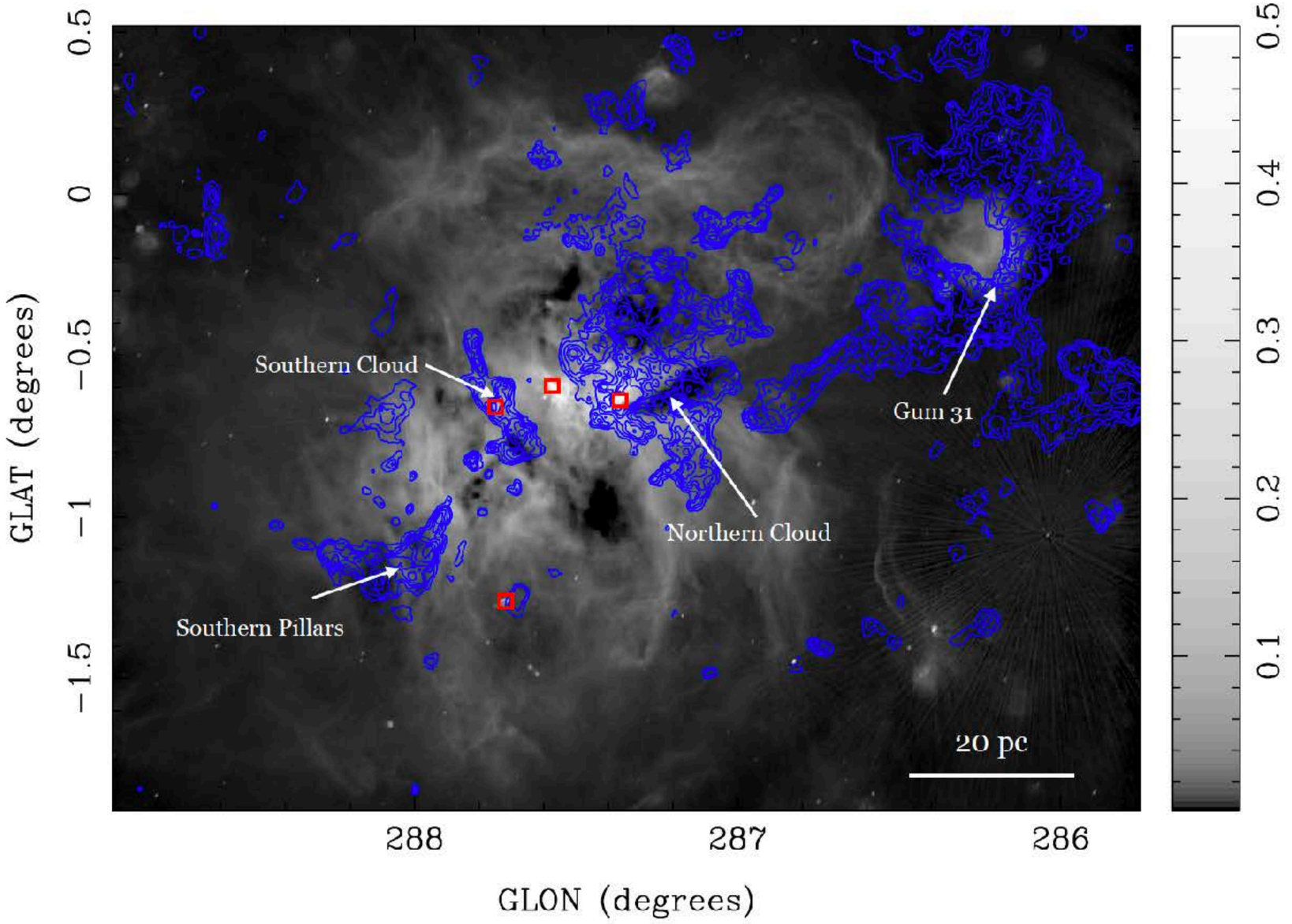

FIG. 9.— Map of the CO($1 \rightarrow 0$) molecular line from Paper I (contour map) overlaid on the 1 – 3 GHz radio continuum emission map (background black and white map). Contour levels are 4, 8 ,16, 25, 36, 49, and 64 K km s^{-1}. Color bar is in Jy/beam. This figure also shows the four main clouds identified in Paper I, the Southern Pillars, Southern Cloud, Northern Cloud and Gum 31. Red squares show the regions used to extract the spectra shown in Figure 7.

8um & 70umとの比較

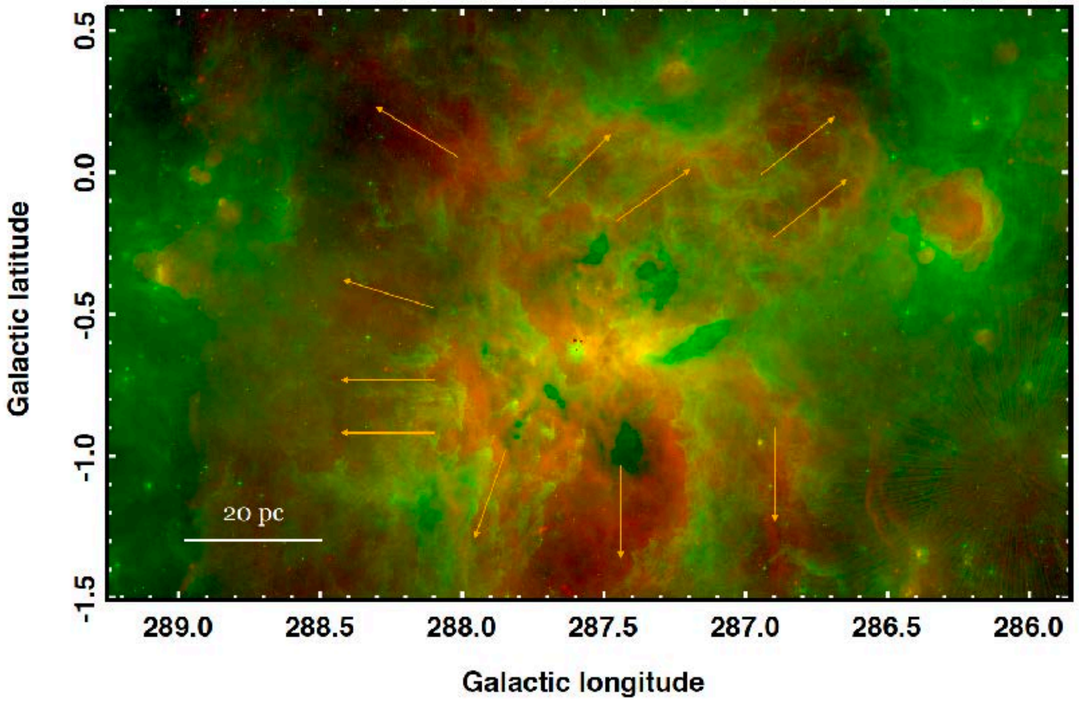

FIG. 10.— Color composite image of the CNC-Gum 31 complex. Green shows the *Spitzer* IRAC 8 μm map, while red shows the ATCA continuum image. A clear spatial anti-correlation between the two tracers is observed, with the radio continuum emission filling the cavities observed in the 8 μm map. The 8 μm map traces the PAH emission, so it will be bright on the cloud's surfaces. Orange arrows show the apparent direction of the hot gas traced by the radio continuum map as it permeates through the denser gas, illuminating the cloud surfaces as traced by PAH emission.

8um: green
1-3GHz: red

70um: Cyan
1-3GHz: red

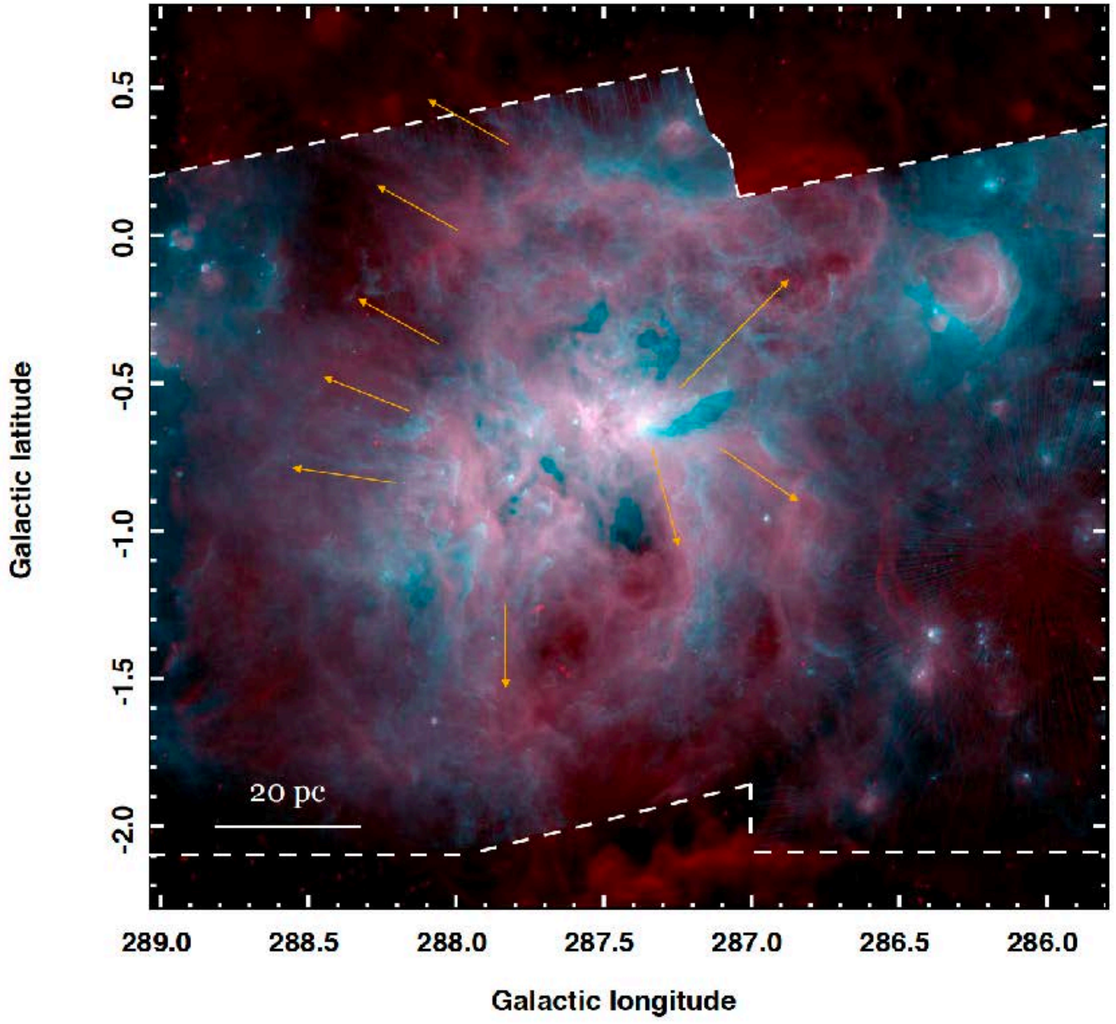

FIG. 11.— Color composite image of the CNC-Gum 31 complex. Cyan shows the *Herschel* 70 μm map, while red shows the ATCA continuum image. The dashed white line shows the 70 μm map coverage. Pink color shows regions where both 70 μm and radio continuum map emission are present, marking the location where dust has been locally warmed by the radiation field. The orange arrows show the approximate direction of the hot gas as it permeates through the CNC molecular complex, and escapes towards the Galactic Plane.

Some small-scale structures

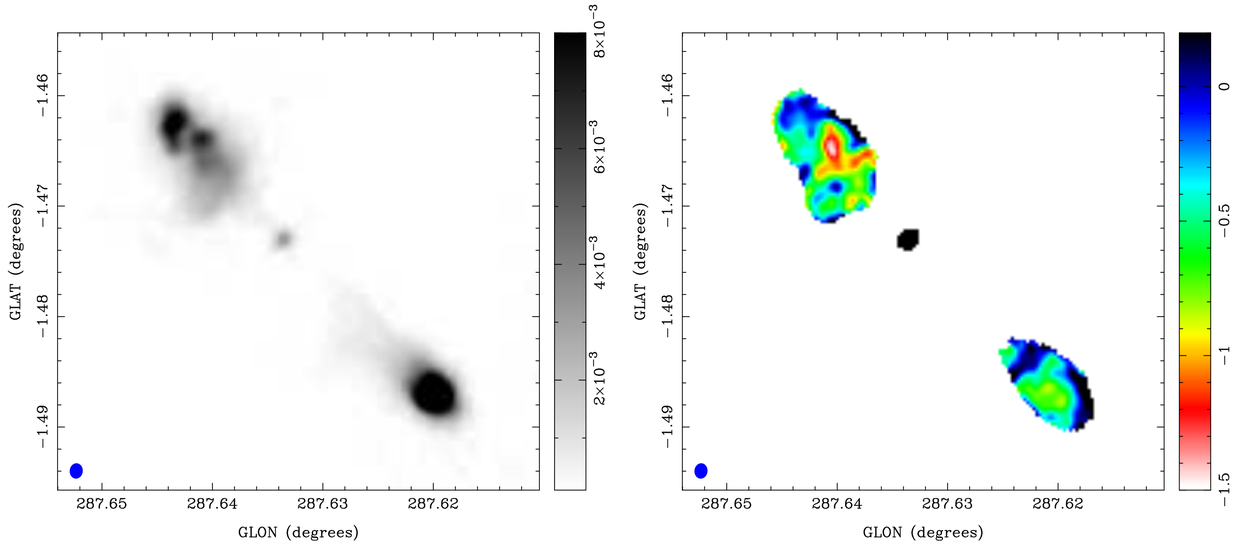

FIG. 13.— Left: 1−3 GHz radio continuum emission map of the object with an identified bipolar outflow/jet structure. The image was created using multi-terms and wide frequency imaging with the CASA task *tclean*. The color bar is in Jy/beam. We identified a clear central source, with a bipolar emission structure, similar to FR II extragalactic sources. Right: Spectral index map of the region. The values are > –0.5 in the lobes, which are consistent with non-thermal emission in those regions.

Bipolar outflows in 1-3GHz and Sp. Index

HII regions in 1-3GHz (left) and at 3mm (right)

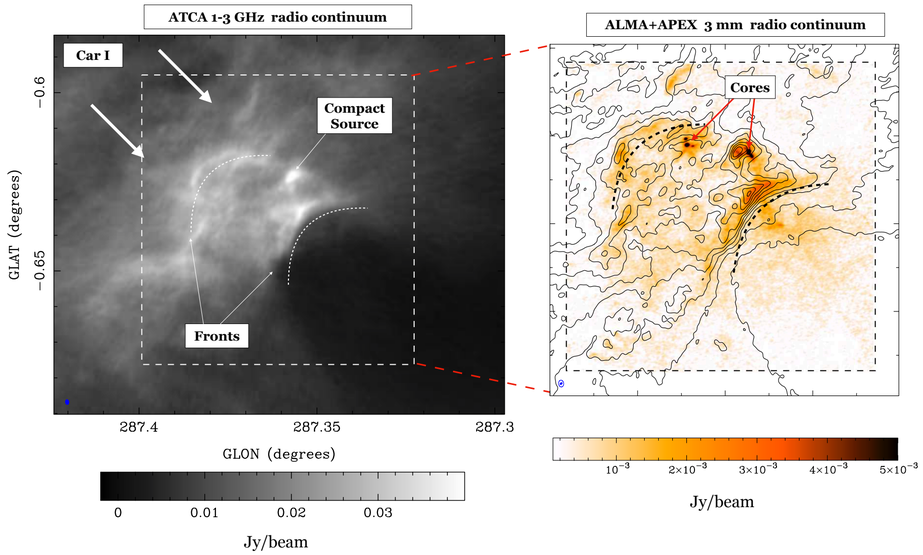

FIG. 14.— Left: ATCA 1 − 3 GHz radio continuum image towards the H II region Car I. This image was generated with robust parameter equal to −0.5 to maximize the spatial resolution. The beam size is $5\farcs6 \times 4\farcs1$. White arrows show the approximate direction of the radiation from massive stars in the Trumpler 14 cluster. The white dashed arcs show the regions where we identified ionization fronts in ALMA 3 mm continuum data (Rebolledo et al. 2020). Right: ALMA + APEX combined continuum image at 3 mm from Rebolledo et al. (2020). Black contours shows the 1 − 3 GHz radio continuum emission, with levels of 4 mJy/beam $\times k$ starting at 4 mJy/beam, with k = 1, 2, 3, 4, 5, 6, 7, 8, and 9. The black dashed box shows the region covered by ALMA observations. The black dashed arcs shows the ionization front in left panel. Red arrows shows the position of the resolved cores identified in our ALMA 3 mm continuum data.

16. Chemical analysis of early-type stars with planets

C. Saffe, P. Miquelarena, J. Alacoria, M. Flores, M. Jaque Arancibia, D. Calvo, G. Martín Girardi, M. Grosso, A. Collado Aims. To explore the chemical pattern of early-type stars with planets, searching for a possible signature of planet formation. In particular, we study a likely relation between the lambda Bootis chemical pattern and the presence of giant planets. Methods. We performed a detailed abundance determination in a sample of early-type stars with and without planets via spectral synthesis. Results. We compared the chemical pattern of the stars in our sample (13 stars with planets and 24 stars without detected planets) with those of lambda Bootis and other chemically peculiar stars. We have found four lambda Bootis stars in our sample, two of which present planets and circumstellar disks (HR 8799 and HD 169142) and one without planets detected (HD 110058). We have also identified the first lambda Bootis star orbited by a brown dwarf (zeta Del). This interesting pair lambda Bootis star + brown dwarf could help to test stellar formation scenarios. We found no unique chemical pattern for the group of early-type stars bearing giant planets. However, our results support, in principle, a suggested scenario in which giant planets orbiting pre-main-sequence stars possibly block the dust of the disk and result in a lambda Bootis-like pattern. On the other hand, we do not find a lambda Bootis pattern in different hot-Jupiter planet host stars, which do not support the idea of possible accretion from the winds of hot-Jupiters, recently proposed in the literature. Then, other mechanisms should account for the presence of the lambda Bootis pattern between main-sequence stars. Finally, we suggest that the formation of planets around lambda Bootis stars such as HR 8799 and HD 169142 is also possible through the core accretion process and not only gravitational instability [abridged]

- λ Bootis (うしかい座) star：金属量が太陽に比べ1/10低い特異な化学組成を持つA型星
  - ~2% of B-F MS, but ~33% of Herbig Ae/Be stars，起源は謎.
- 惑星がある星13個とない星24個で大気化学組成を詳細に探査，λ Boo 型星との関連調査
  - 4つ(+λ Boo)がλ Boo型，うち2つが惑星・星周円盤付き（HR 8799, HD169142）
  - 他のうち1つはBD付随 (zeta Del)，他の1つは惑星なし(HD 110058)
- 惑星があるとダストの流入が妨げられた結果かも．．．はっきりしたことは言えないが
- Hot Jupiter からのウインドが中心星に降着したと言う説とは合致しない（特段の差が見られない）

今回のサンプルと観測諸元

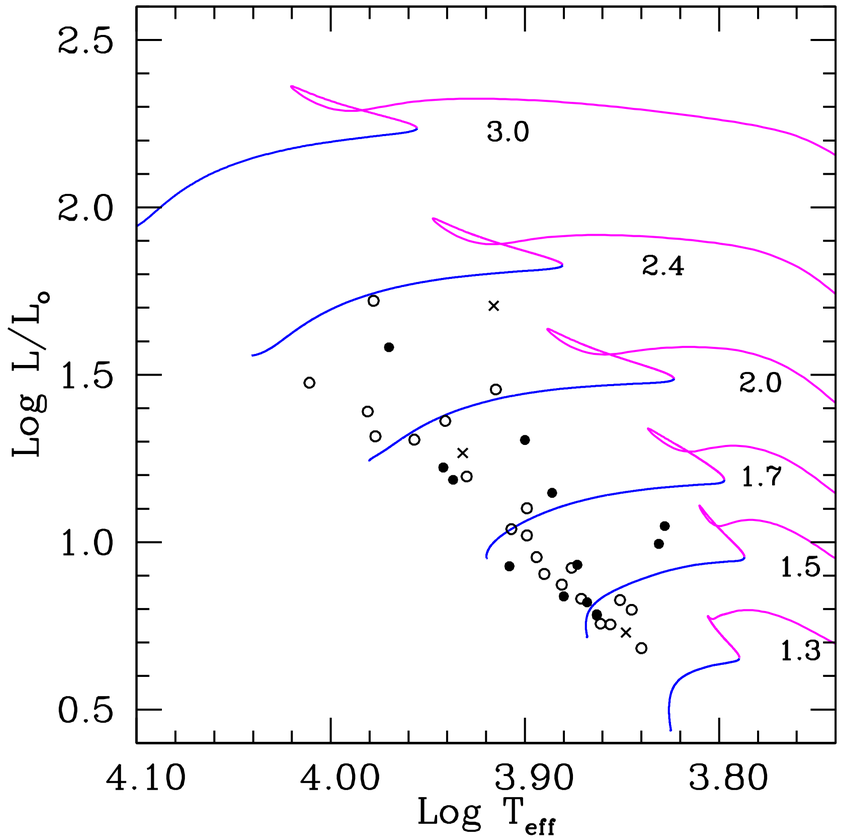

Fig. 1. Effective temperature versus luminosity for stars with planets, without planets and with a BD companion (filled circles, empty circles and crosses). Evolutionary tracks for stars of different masses are showed in blue/magenta for main-sequence/evolved stars. The numbers are expressed in solar masses.

Table 1. General characteristics of the spectrographs used in this work.

Instrument	R	CCD Detector	Pixel size	Telescope	Approx. Wave. Range
HARPS	115000	4k x 4k	15 μm	La Silla 3.6m	3800 - 6800
HARPS-N	115000	4k x 4k	15 μm	TNG 3.6m	3800 - 6800
HIRES	67000	2k x 4k	15 μm	Keck 10m	3750 - 9000
SOPHIE	75000	4k x 2k	15 μm	OHP 1.93m	3900 - 6800
ELODIE	42000	1k x 1k	24 μm	OHP 1.93m	3850 - 6800
REOSC	13000	1k x 1k	24 μm	CASLEO 2.1m	3800 - 6000

Star name	Spectral Type	Companion Detection Method	Companion Mass [M_{Jup}]	Companion Type	IR Excess	Spectra	S/N @5000 Å	Companion & IR Excess Refs.
Exoplanet host stars								
β Pic	A6V	Imaging	9.9, 8.9	Planet	Yes	HARPS	1500	R1, R14, R20, R21
Fomalhaut	A4V	Imaging	< 1	Planet	Yes	REOSC	490	R2, R20, R21
KELT-9	B9.5 – A0	Transit	2.88	Planet	No	HARPS-N	550	R3, R23
HD 95086	A8III	Imaging	2.6	Planet	Yes	HARPS	310	R4, R14, R24, R25
HD 169142	F1VekA3mA3 HAeBe	Imaging	< 1, < 10	Planet	Yes	HARPS	210	R5, R26
HR 8799	F0+VkA5mA5	Imaging	8.3, 8.3, 9.2	Planet	Yes	ELODIE	370	R6, R14, R27, R28
KELT-17	A2	Transit	1.31	Planet	No	REOSC	210	R7
KELT-20	A0	Transit	3.5	Planet	No	HARPS-N	450	R8
MASCARA-1	A8	Transit	3.7	Planet	...	HARPS-N	560	R9
WASP-33	kA5hA8mF4	Transit	< 4.1	Planet	...	HIRES	250	R10
HAT-P-49	A8	Transit	1.73	Planet	...	SOPHIE	135	R15
WASP-167	F1V	Transit	< 8	Planet	...	HARPS	205	R16
WASP-189	A4/5IV/V	Transit	1.99	Planet	...	HARPS	1105	R17
Stars with a brown dwarf (BD) companion								
β Cir	A3Va	Imaging	58.7	BD	Yes	HARPS	250	R11, R22
59 Dra	A7 HAeBe	RV	25	BD	...	ELODIE	350	R12
ζ Del	A3Va	...	50	BD	...	ELODIE	290	R18
Stars with no-companion detected								
HD 133803	F2IVm-2	...	...	...	...	HARPS	300	R14
HR 4502 A	A0V	...	...	...	...	HARPS	130	R14
BU Psc	A9V/IV	...	...	...	...	HARPS	110	R14
HD 29391	F0 IV	...	...	...	...	HARPS	410	R14
HD 105850	A1V	...	...	...	...	HARPS	650	R14
HD 110058	A0V	...	...	...	Yes	HARPS	450	R14, R29
HD 115820	A7/8V	...	...	...	...	HARPS	250	R14
HD 120326	F0V	...	...	...	...	HARPS	200	R14
HD 129926	F0VSr+G1V	...	...	...	...	HARPS	600	R14
HD 146624	A1 Va	...	...	...	...	HARPS	620	R14
HD 153053	A5IV/V	...	...	...	Yes	HARPS	600	R14, R22
HD 156751	A7II/III	...	...	...	...	HARPS	410	R14
HD 159492	A5IV/V	...	...	...	Yes	HARPS	720	R14, R22
HD 188228	A0Va	...	...	...	Yes	HARPS	840	R14, R21
HD 23281	A5III/IV	...	...	...	...	HARPS	470	R14
HD 50445	A3V	...	...	...	...	HARPS	680	R14
HD 56537	A4IV	...	...	...	Yes	HARPS	620	R14, R20
HD 88955	A2Va	...	...	...	Yes	HARPS	590	R14, R20
V435 Car	A5V	...	...	...	Yes	HARPS	200	R14
λ Boötis	A0Va lBoo	...	...	...	Yes	ELODIE	525	R20, R21
Vega	A0Va	...	...	...	Yes	SOPHIE	1230	R19, R20, R21

13

3

21

今回求められた星の基本パラメータ

Star	T_{eff} [K]	log g [dex]	v_{micro} [km s^{-1}]	$v \sin i$ [km s^{-1}]
β Pic	8084 ± 130	4.22 ± 0.13	3.31 ± 0.83	113.0 ± 1.3
Fomalhaut	8745 ± 195	4.17 ± 0.10	2.95 ± 0.74	82.0 ± 3.2
KELT-9	9329 ± 118	4.00 ± 0.14	2.27 ± 0.57	113.5 ± 4.6
HD 95086	7593 ± 122	4.02 ± 0.14	3.09 ± 0.77	30.0 ± 1.4
HD 169142	7296 ± 365	4.20 ± 0.25	2.75 ± 0.69	55.0 ± 0.8
HR 8799	7301 ± 190	4.12 ± 0.23	2.76 ± 0.69	50.5 ± 1.0
KELT-17	7471 ± 210	4.20 ± 0.14	2.50 ± 0.63	43.0 ± 0.6
KELT-20	8652 ± 160	4.11 ± 0.20	3.03 ± 0.76	111.0 ± 3.1
MASCARA-1	7687 ± 238	4.09 ± 0.14	3.17 ± 0.79	99.0 ± 3.9
WASP-33	7373 ± 164	4.14 ± 0.20	2.86 ± 0.71	82.5 ± 2.0
HD 133803	6998 ± 193	4.08 ± 0.23	2.29 ± 0.57	89.5 ± 1.3
β Cir	8552 ± 297	3.94 ± 0.18	3.12 ± 0.78	61.0 ± 0.8
59 Dra	7053 ± 194	4.18 ± 0.21	2.38 ± 0.60	53.0 ± 1.1
HR 4502 A	9569 ± 253	4.00 ± 0.16	1.96 ± 0.49	18.5 ± 0.7
BU Psc	7185 ± 160	4.22 ± 0.14	2.59 ± 0.65	53.0 ± 2.6
HD 29391	7259 ± 167	4.12 ± 0.20	2.70 ± 0.68	70.0 ± 1.7
HD 105850	9052 ± 167	4.08 ± 0.08	2.61 ± 0.65	125.0 ± 1.5
HD 110058	7839 ± 202	4.00 ± 0.14	3.26 ± 0.81	153.5 ± 2.9
HD 115820	7610 ± 135	4.30 ± 0.15	3.11 ± 0.78	92.2 ± 1.8
HD 120326	6925 ± 143	4.37 ± 0.11	2.17 ± 0.54	66.5 ± 1.5
HD 129926	7101 ± 167	4.18 ± 0.20	2.46 ± 0.62	113.0 ± 2.1
HD 146624	9489 ± 184	4.13 ± 0.07	2.06 ± 0.52	34.0 ± 0.5
HD 153053	7916 ± 129	4.03 ± 0.14	3.29 ± 0.82	103.0 ± 1.6
HD 156751	7432 ± 175	3.92 ± 0.21	2.93 ± 0.73	100.0 ± 4.3
HD 159492	8076 ± 128	4.24 ± 0.13	3.31 ± 0.83	52.3 ± 1.2
HD 188228	10262 ± 172	4.29 ± 0.06	1.17 ± 0.29	83.0 ± 3.5
HD 23281	7761 ± 135	4.18 ± 0.15	3.22 ± 0.80	77.7 ± 2.4
HD 50445	7922 ± 117	4.03 ± 0.14	3.29 ± 0.82	96.0 ± 1.9
HD 56537	8231 ± 122	3.70 ± 0.12	3.29 ± 0.82	146.0 ± 4.3
HD 88955	8733 ± 154	3.76 ± 0.10	2.96 ± 0.74	99.0 ± 3.0
V435 Car	7510 ± 165	4.21 ± 0.14	3.01 ± 0.75	106.4 ± 1.9
HAT-P-49	6730 ± 234	4.02 ± 0.14	1.82 ± 0.46	14.8 ± 0.2
λ Boötis	8512 ± 144	3.95 ± 0.06	3.15 ± 0.79	115.0 ± 3.1
Vega	9505 ± 188	3.95 ± 0.19	2.04 ± 0.51	20.5 ± 0.7
WASP-167	6770 ± 210	4.05 ± 0.14	1.90 ± 0.47	52.0 ± 2.0
WASP-189	7946 ± 136	3.85 ± 0.12	3.30 ± 0.82	95.2 ± 3.3
ζ Del	8236 ± 124	3.60 ± 0.12	3.29 ± 0.82	108.0 ± 3.6

有効温度

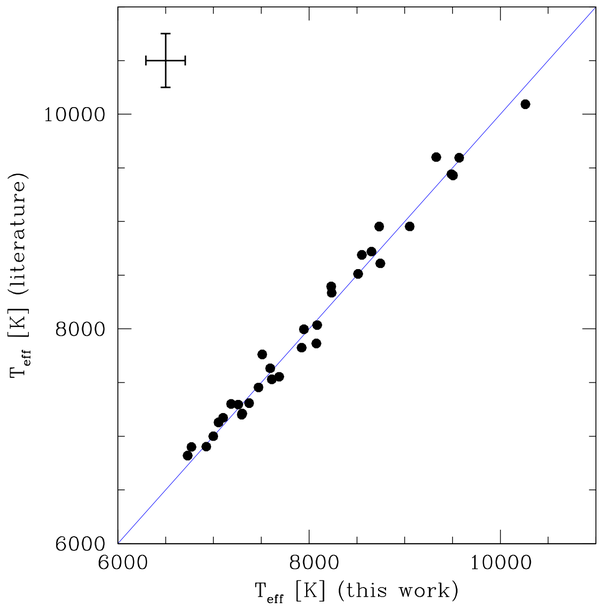

Fig. 2. Effective temperature T_{eff} derived in this work versus literature data. Average dispersion bars are showed in the upper left corner of the panel.

v sin i

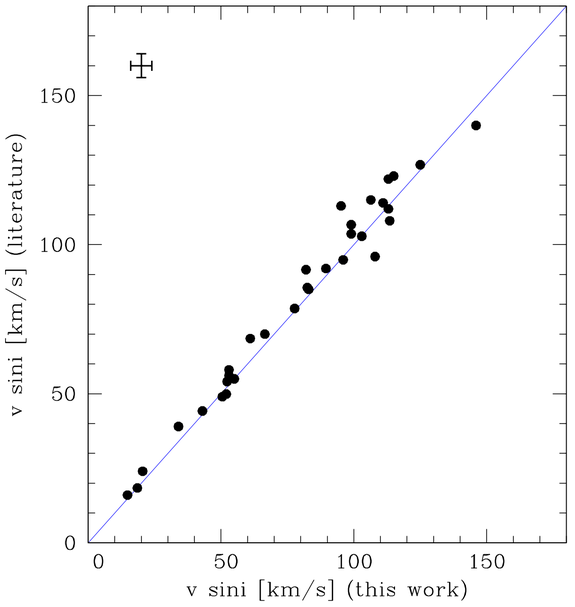

Fig. 3. Projected rotational velocity $v \sin i$ derived in this work versus literature data. Average dispersion bars are showed in the upper left corner of the panel.

Abundance analysis & spectra fit

- 黒が観測，青が合成したスペクトル，赤が差
- 赤が今回同定されたλBoo型．λBooは青

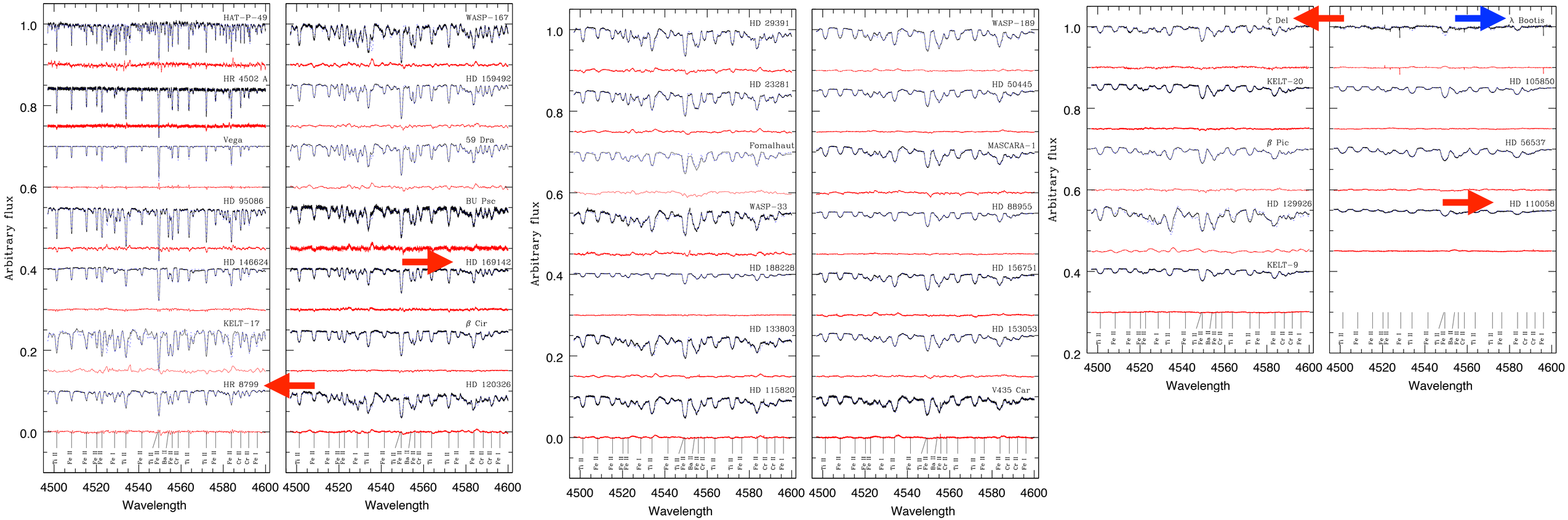

. Observed, synthetic and difference spectra (black, blue dotted and red lines) for the stars in our sample, sorted by $v \sin i$.

今回見つけたλ Boo型の abundance pattern

HR8799は惑星あり

HD169142 はリングギャップを含む円盤が付随

ζ Delは912au付近にBD付随

HD110058は特段の兆候なし

一部の研究者は，HR8799のようにmetal Poorな星周りの惑星形成はGIによると主張しているが，単にダスト降着を妨げた結果なのかもしれない．

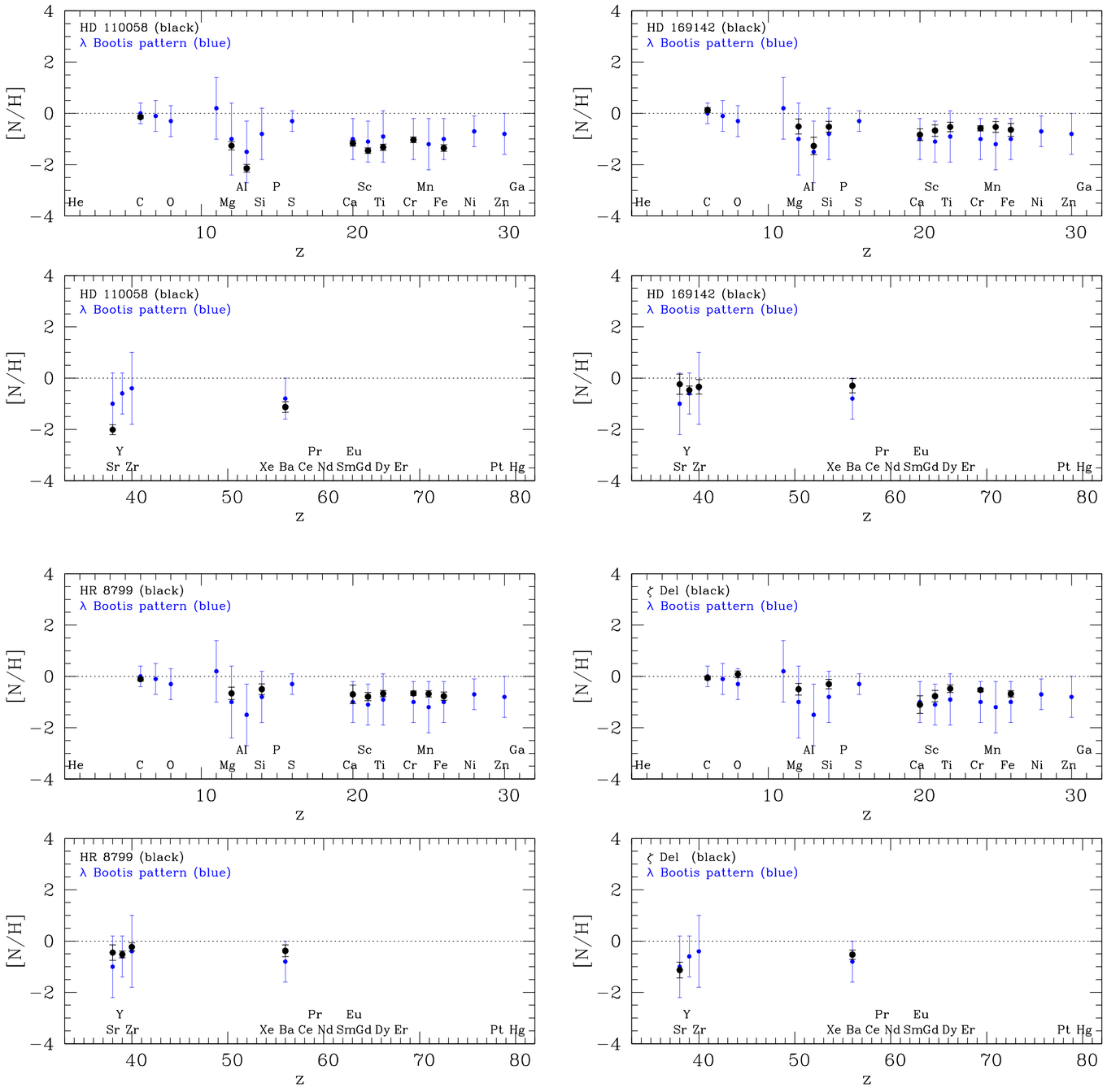

One more but less clear star (HD156751) & λ Boo自身

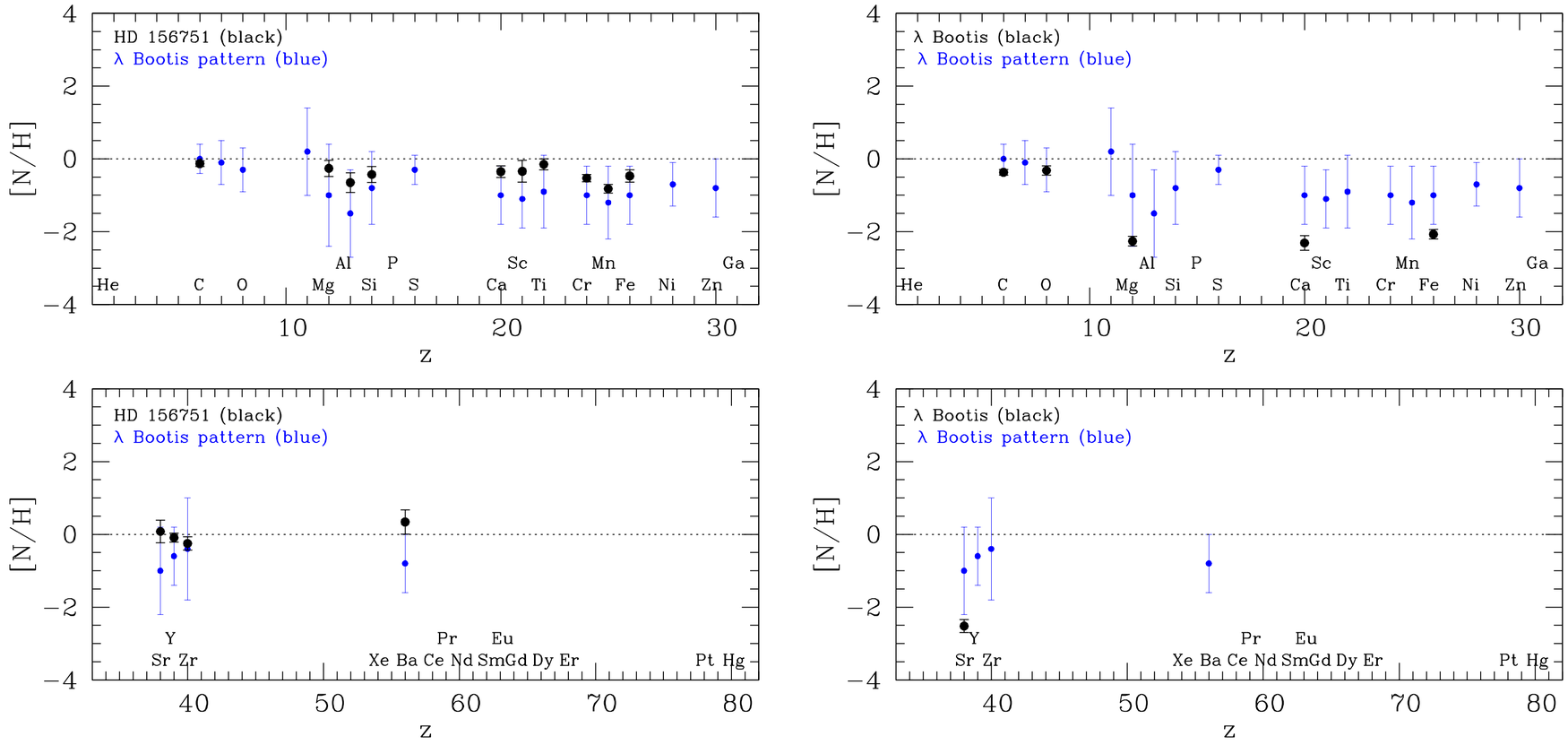

- どちらも，これまで惑星の兆候は得られていない
- 若い方がλ Boo型の割合が多いと知られていたが，HD169142 (HAe) や HR8799(42±5Myr)が該当したが，β PicやHD96086 (<50Myr)は違った

その他

- Hot Jupiter とλ Boo現象が関係していると言う説があったが，今回得られたサンプル（７個）ではそのような兆候は見られない

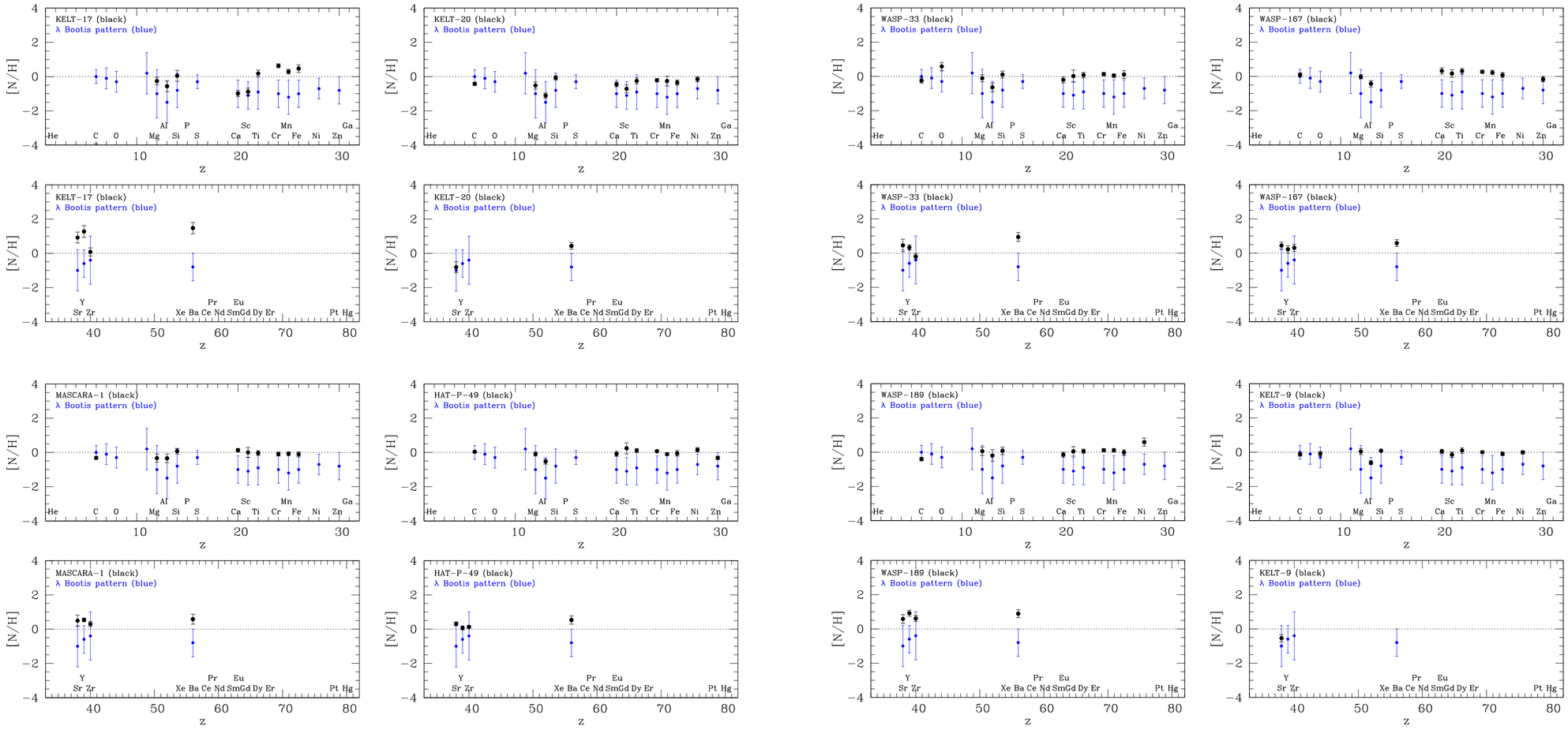

18.

Characterizing the line emission from molecular clouds. Stratified random sampling of the Perseus cloud

M. Tafalla, A. Usero, A. Hacar *Context*. The traditional approach to characterize the structure of molecular clouds is to map their line emission. *Aims*. We aim to test and apply a stratified random sampling technique that can characterize the line emission from molecular clouds more efficiently than mapping. *Methods*. We sampled the molecular emission from the Perseus cloud using the H2 column density as a proxy. We divided the cloud into ten logarithmically spaced column density bins, and we randomly selected ten positions from each bin. The resulting 100 cloud positions were observed with the IRAM 30m telescope, covering the 3mm-wavelength band and parts of the 2 and 1mm bands. *Results*. We focus our analysis on 11 molecular species detected toward most column density bins. In all cases, the line intensity is tightly correlated with the H2 column density. For the CO isotopologs, the trend is relatively flat, while for high-dipole moment species such as HCN, CS, and HCO+ the trend is approximately linear. We reproduce this behavior with a cloud model in which the gas density increases with column density, and where most species have abundance profiles characterized by an outer photodissociation edge and an inner freeze-out drop. The intensity behavior of the high-dipole moment species arises from a combination of excitation effects and molecular freeze out, with some modulation from optical depth. This quasi-linear dependence with the H2 column density makes the gas at low column densities dominate the cloud-integrated emission. It also makes the emission from most high-dipole moment species proportional to the cloud mass inside the photodissociation edge. *Conclusions*. Stratified random sampling is an efficient technique for characterizing the emission from whole molecular clouds. It shows that despite the complex appearance of Perseus, its molecular emission follows a relatively simple pattern.

ペルセウス座分子雲をターゲットに以下を実施

方法

- 分子雲構造を探る際，マップするのではなく，階層的ランダムサンプリングで特徴づけられないかを試験
- H_2柱密度の10binそれぞれに10標本点(計100点)，λ=3mmバンド全体と2mm & 1mmバンド一部をIRAM 30mでカバー
- 11molecular species + isotopologues解析
  - ほぼ全てのbinで検出
  - 様々なdipole moment μ (← critical density)

結果と考察

- Line intensityはH_2柱密度と正の相関
  - COはわりとflat
  - μが大きいspeciesほどlinearに近づく (HCN, CS, HCO+, HNC)
- 以下の組み合わせで簡単に振る舞いを理解
  - 励起効果
  - Edge (光解離) - Center (凍結)で線形補間
  - Optical depthによる変調をちょっぴり

標本点の位置(左)と柱密度

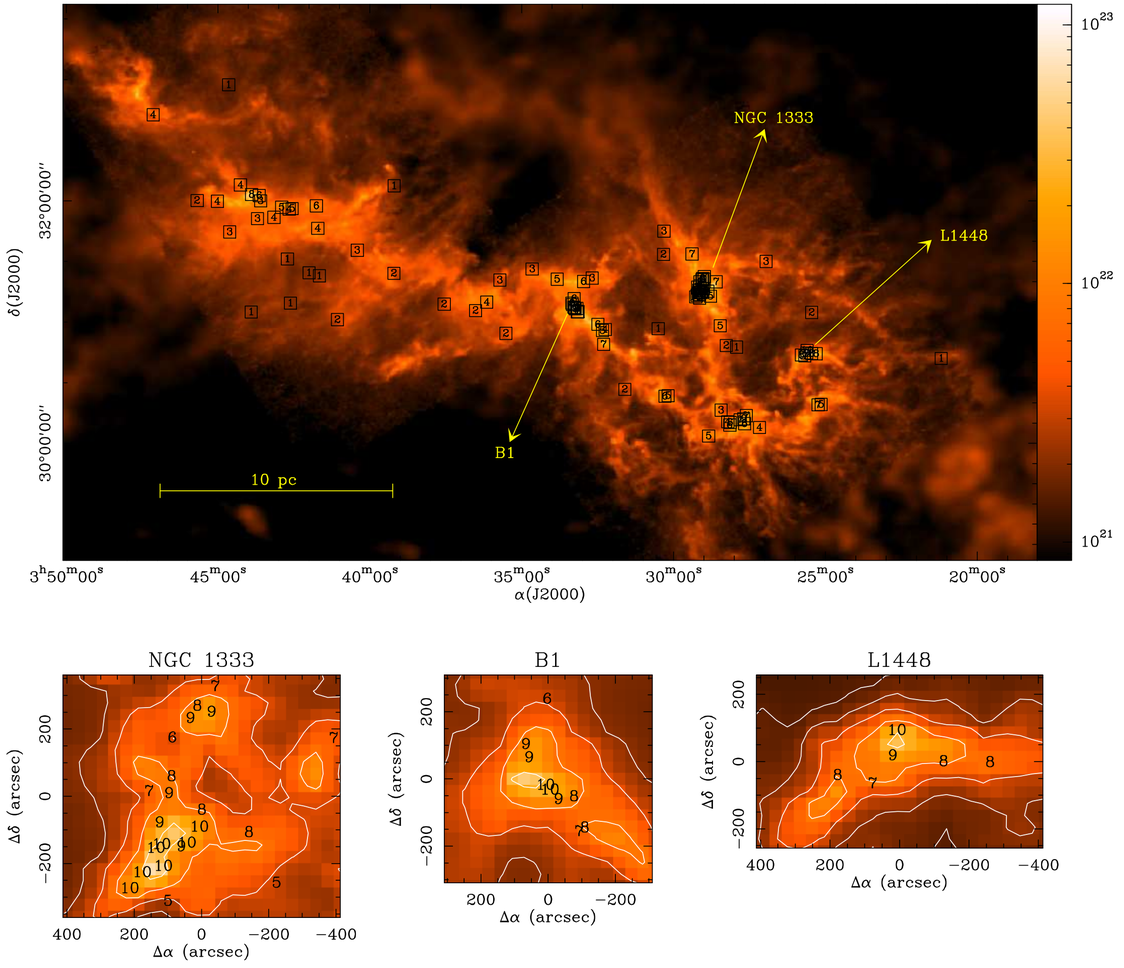

Fig. 1. Sampling of the Perseus cloud. *Top:* H_2 column density map of the Perseus molecular cloud from Zari et al. (2016) with squares indicating the location of the 100 positions selected to characterize the line emission from the cloud using stratified random sampling. The number in each square indicates the column density bin to which the position belongs, and ranges from 1 (lowest column density) to 10 (highest). *Bottom:* Expanded view of the three regions that concentrate most of the high column density positions, and that correspond to the well-known star-forming regions NGC 1333, B1, and L1448. Contours are in units of $N(H_2)$, start at 1.25×10^{21} cm^{-2}, and increase by factors of 2.5. The 10 pc scale bar assumes a distance of 300 pc.

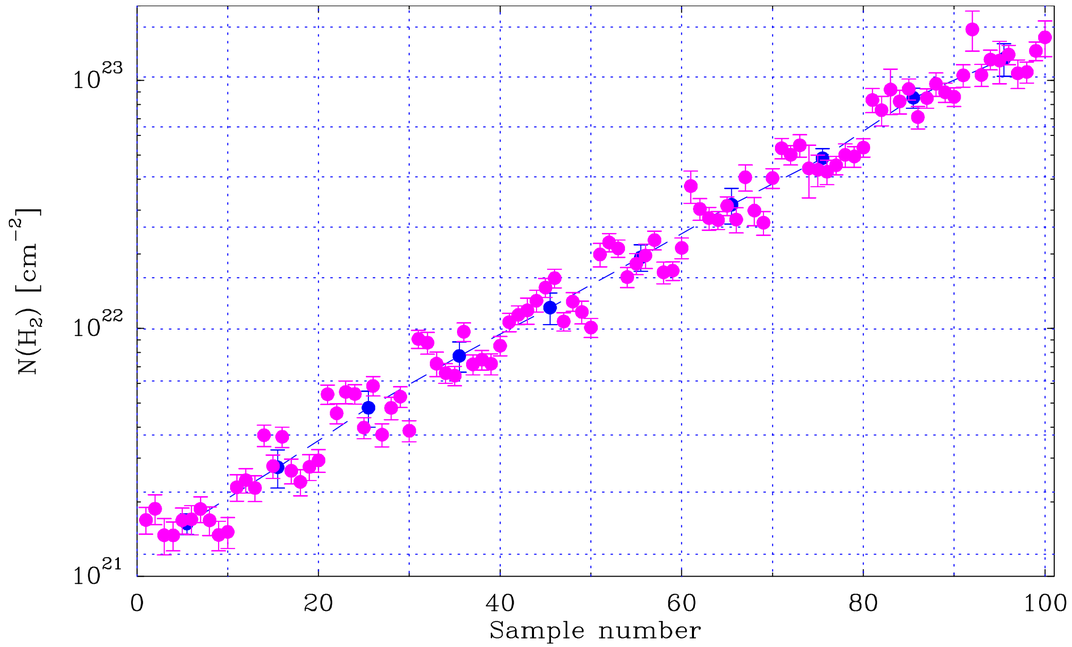

Fig. 2. H_2 column density as a function of sample number for the 100 positions randomly chosen to represent the Perseus molecular cloud (magenta circles). The dashed horizontal lines mark the boundaries of the ten column-density bins in which the cloud was divided, and the vertical lines enclose the ten points chosen to sample each bin. The blue circles indicate the geometrical mean of the H_2 column densities inside each bin, and their error bars indicate their dispersion. All values derived from Zari et al. (2016) data.

COMPLETEとの比較：CO isotopologues

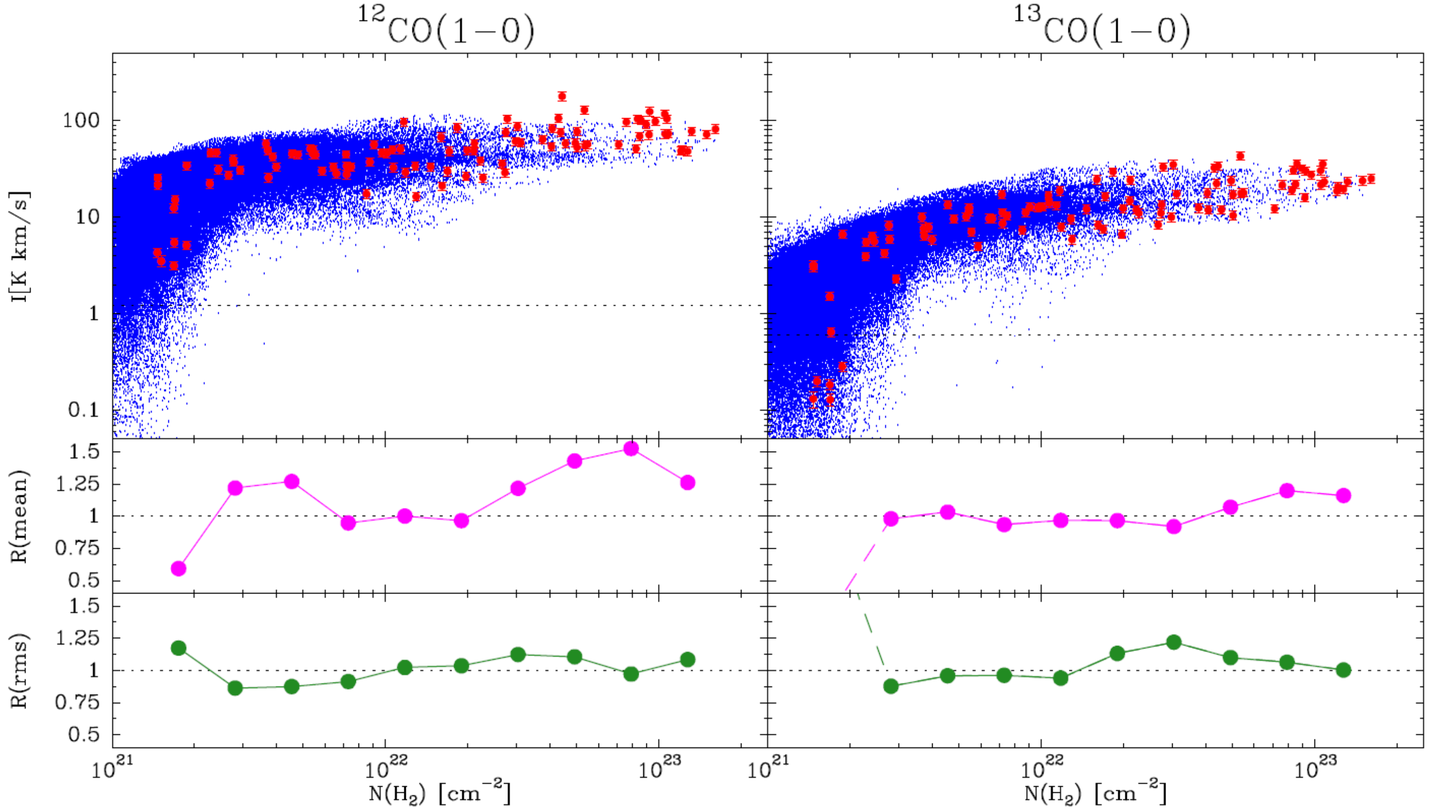

Fig. 3. Comparison between sampling observations and COMPLETE full maps for ^{12}CO(1–0) and ^{13}CO(1–0). *Top panels:* Scatter plots of the integrated intensity as a function of $N(H_2)$. The blue dots represent the results from the COMPLETE maps presented by Ridge et al. (2006) and each of them contains more than 2×10^5 spectra. The red symbols represent the 100 measurements obtained using stratified random sampling. The dotted lines mark the 3σ detection level of the COMPLETE maps. *Middle panels:* Ratio between the mean intensity derived using the sampling data and the COMPLETE maps for each of the ten $N(H_2)$ bins in which the cloud was divided. For ^{13}CO(1–0), the measurement in lowest $N(H_2)$ bin is not reliable since the sampling data show that the intensity often lies below the COMPLETE detection limit. *Bottom panels:* Ratio between the rms derived using the sampling data and the COMPLETE maps. As with the mean values, the ^{13}CO(1–0) measurement for the lowest $N(H_2)$ bin lies below the detection limit, so the rms estimate is not reliable. We note how both the mean and rms ratios for the two CO isotopologs lie in the vicinity of 1, indicating that the sampling method allows estimating the main emission parameters with an accuracy of about 50-20% depending on the parameter.

青がCOMPLETE

赤が本研究

結果(1)：CO

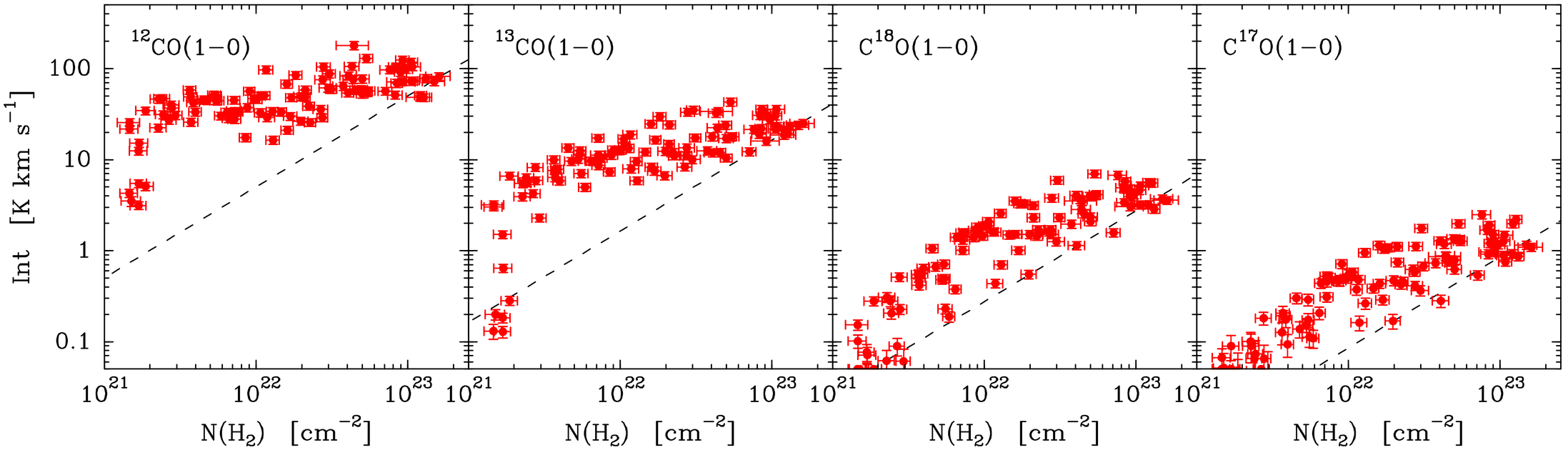

Fig. 4. Integrated line intensity as a function of H_2 column density for the J=1–0 transition of the four main CO isotopologs. For reference, each panel shows a linear relation that fits the average intensity of the highest column density bin (dashed line). Depending on the transition, the lower limit of the intensity scale (0.05 K km s^{-1}) approximately corresponds to one to three times the noise level in the integrated intensity.

結果(2)：large μ species

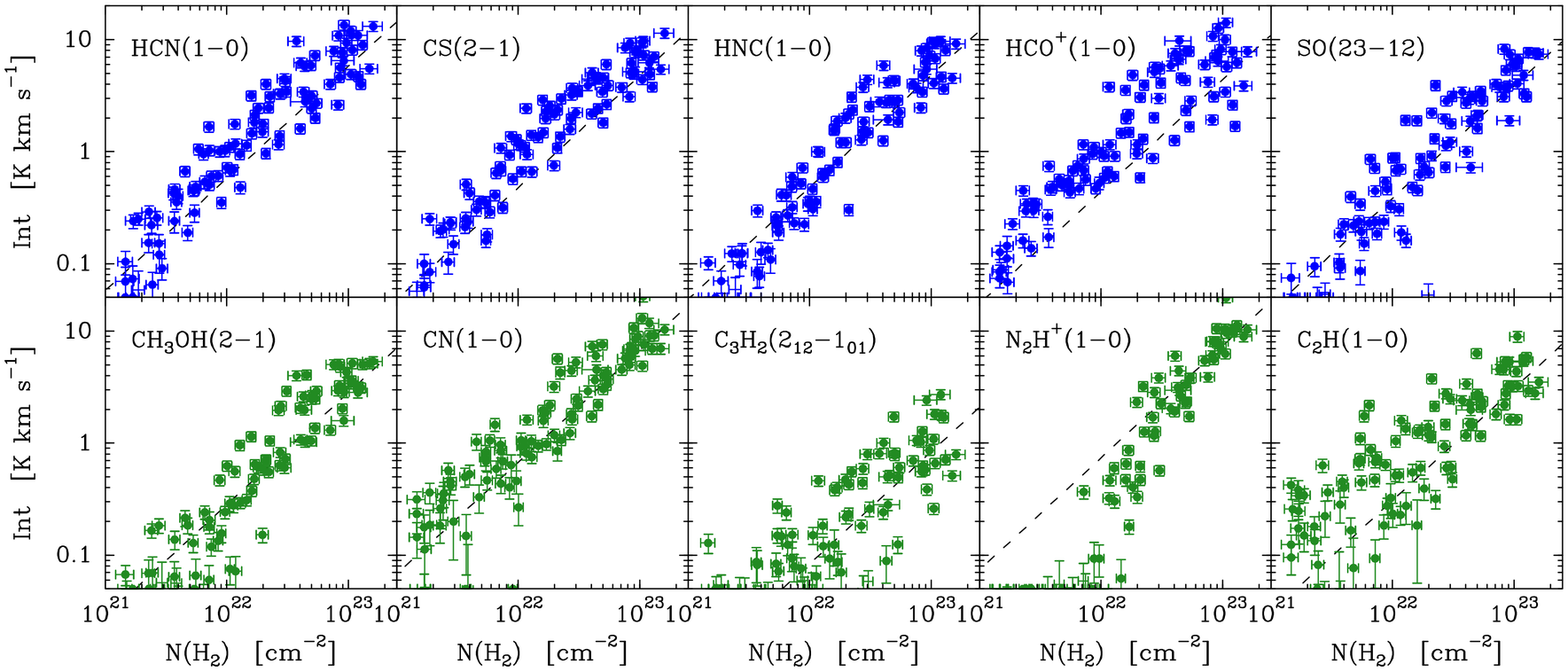

Fig. 5. Integrated line intensity as a function of H_2 column density for the survey species detected in at least five column density bins. *Top:* Traditional dense gas tracers (blue symbols). *Bottom:* Additional tracers of dense gas (green symbols). For reference, each panel shows a linear relation that fits the average intensity of the highest column density bin (dashed line). For HCN(1–0), CN(1–0), N_2H^+(1–0), and C_2H(1–0), the intensity includes the contribution from all detected hyperfine components. For CH_3OH(2–1), the intensity includes the contribution from the A^+ and E components. Depending on the transition, the lower limit of the intensity scale (0.05 K km s^{-1}) approximately corresponds to one to three times the noise level in the integrated intensity.

柱密度 vs. ライン積分強度

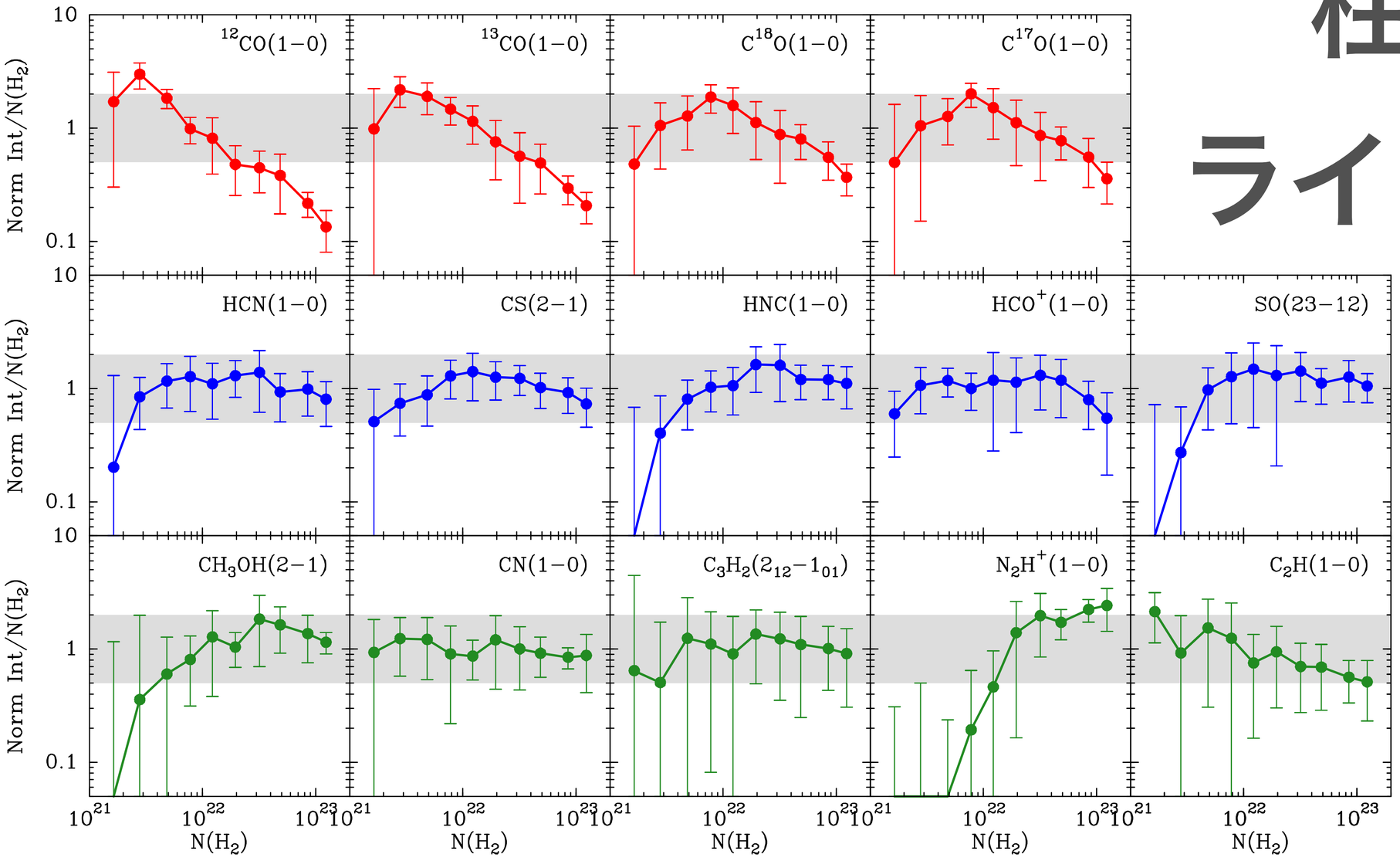

Fig. 7. Normalized ratio between integrated intensity and H_2 column density as a function of H_2 column density. The data points represent bin-averaged values and the error bars represent the rms dispersion. The horizontal gray band encloses the region were deviations from unity are within a factor of 2.

COは基本的に外側で稼ぐ
Large μは比較的全体で稼ぐものが多い

モデルの構築とCOとの比較

- COのJ=2-1と1-0の比からT=11Kで一様
  - 外側のUV photonの加熱はCO解離に使われ大して効かない
- 密度：柱密度の関数で与える．HCNやCSの複数遷移間の比から$N(H_2)^{0.75}$
- 速度分散：C18O(2-1)から$N(H_2)^{0.15}$
- 化学組成は以下の式でパラメータ化

$$X(N(\mathrm{H_2})) = X_0 \times f_{\mathrm{out}}(N(\mathrm{H_2})) \times f_{\mathrm{in}}(N(\mathrm{H_2})), \quad (1)$$

where X_0 represents a constant scaling factor, and f_{out} and f_{in} are two normalized factors that represent abundance changes with respect to X_0 in the outer and inner parts of the cloud (i.e., at low and high H_2 column densities).

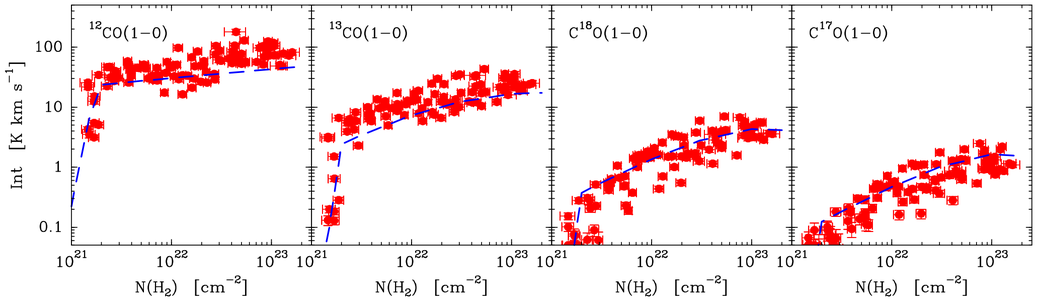

Fig. 10. Comparison between observations and model results for the family of CO isotopologs. The red symbols represent the observed intensities of the J=1–0 line, previously presented in Fig. 4, and the dashed blue lines represent the model results. The sharp drop at low column densities is caused by the photodissociation edge in the abundance profile.

f_{out}: UV解離の影響をPDRモデルで評価，ただし，C_2HやCNはenhance

f_{in}: N_2H以外はdense regionで減少(凍結)，N_2Hは増加（CO凍結との関係で）

モデルとCO以外の分子種の比較

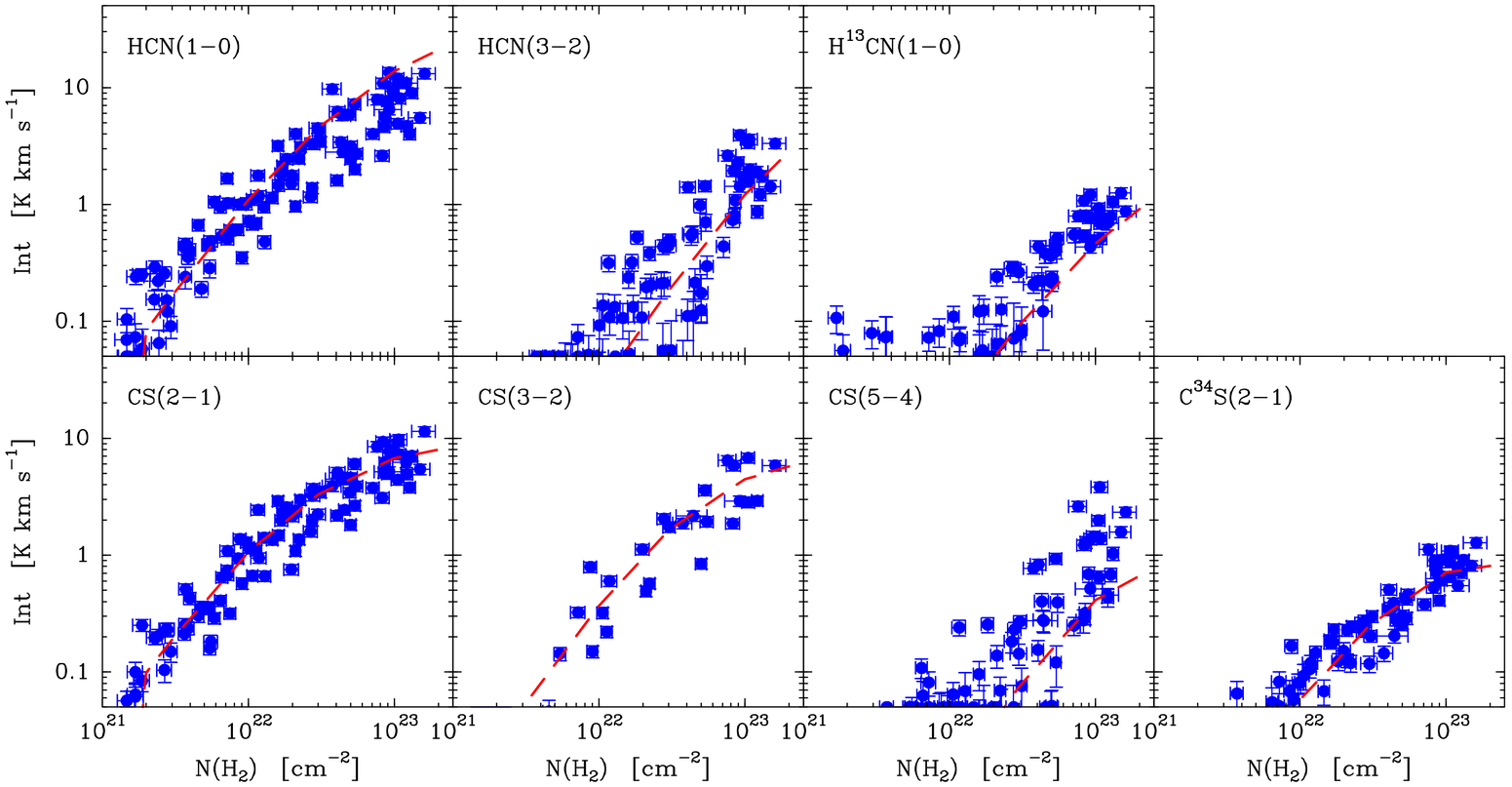

Fig. 11. Comparison between observations and model results for HCN *(top)* and CS *(bottom)*. Each row presents the intensity of the different transitions observed for the species (main and rare isotopologs) as a function of H_2 column density (blue symbols) together with the predictions from the model (dashed red lines). The CS(3–2) dataset has fewer points due to the limited observations carried out in the 2mm-wavelength band. Several $H^{13}CN$(1–0) points can be seen above the plot lower limit at very low column densities. A visual inspection of their spectra suggests that they represent noise or baseline residuals and not true molecular emission.

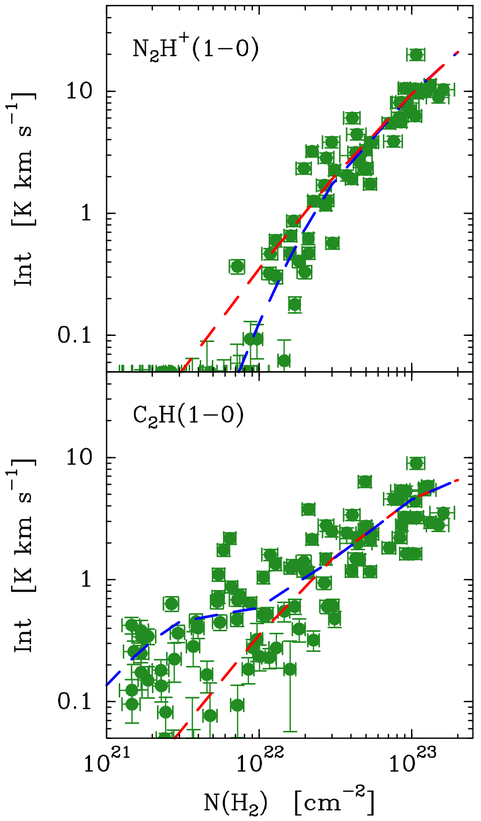

Fig. 12. Comparison between observations and model results for two species that require special abundance profiles: N_2H^+ *(top)* and C_2H *(bottom)*. In both panels, the green symbols represent the observed intensity, previously shown in Fig. 5. In the N_2H^+ panel, the dashed red line represents a constant abundance model that fits the intensity at high column densities. The blue dashed line represents the best-fit model, and includes an internal abundance enhancement. In the C_2H panel, the dashed red line represents a model with no external enhancement, while the blue line represents the externally enhanced best-fit model.

19. Behavior of Hydroxyl Radicals on Water Ice at Low Temperatures

Masashi Tsuge, Naoki Watanabe Because chemical reactions on/in cosmic ice dust grains covered by amorphous solid water (ASW) play important roles in generating a variety of molecules, many experimental and theoretical studies have focused on the chemical processes occurring on the ASW surface. In laboratory experiments, conventional spectroscopic and mass-spectrometric detection of stable products is generally employed to deduce reaction channels and mechanisms. However, despite their importance, the details of chemical reactions involving reactive species (i.e., free radicals) have not been clarified because of the absence of experimental methods for in situ detection of radicals. Because OH radicals can be easily produced in interstellar conditions by not only the photolysis and/or ion bombardments of H2O but also the reaction of H and O atoms, they are thought to be one of the most abundant radicals on ice dust. In this context, the development of a close monitoring method of OH radicals on the ASW surface may help to elucidate the chemical reactions occurring on the ASW surface.

（このアブストラクトは3つの段落のうち一段落目しかない）

- 低温下でのHydroxyl radicalsのアモルファス氷(ASW)表面での振る舞いに関連し．筆者自身が開発した，ASW表面のOHラジカル検出法を用いて，λ=532nmの光子一つでOHがdesorotionすることを確認.
- 氷表面のOHは容易に電子を引き寄せ，OH^-になる．今回はさらに，OH^-の形成がnegative currentを誘起することを突き止め，proton-transferのmirror imageとして100年前に予言されていたproton-hole transfer (Grotthuss mechanism)で実効的に氷内で素早く輸送されることを明かした.
- 低温下の氷マントルでは起こらないと思われていた関連反応が重要になる可能性がある.

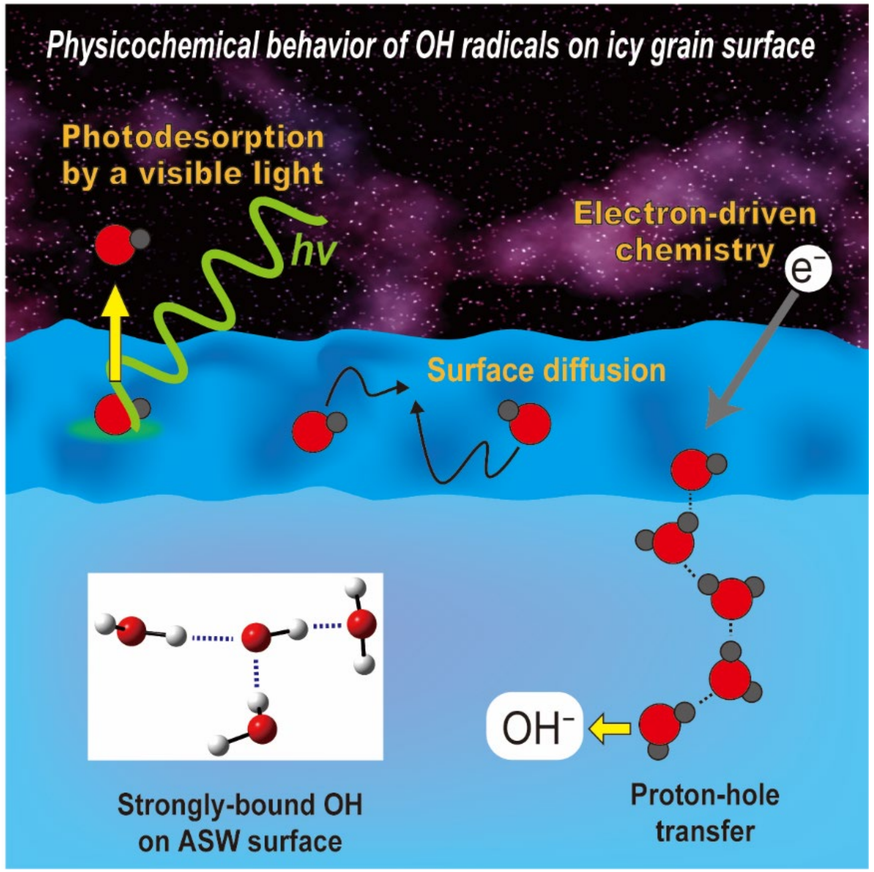

17.

ALMA observations of the early stages of substellar formation in the Lupus 1 and 3 molecular clouds

A. Santamaría-Miranda, I. de Gregorio-Monsalvo, A. L. Plunkett, N. Huélamo, C. López, Á. Ribas, M. R. Schreiber, K. Mužić, A. Palau, L. B. G. Knee, A. Bayo, F. Comerón, A. Hales

The dominant mechanism leading to the formation of brown dwarfs (BDs) remains uncertain. The most direct keys to formation, which are obtained from younger objects (pre-BD cores and proto-BDs), are limited by the very low number statistics available. We aim to identify and characterize a set of pre- and proto-BDs as well as Class II BDs in the Lupus 1 and 3 molecular clouds to test their formation mechanism. We performed ALMA band 6 (1.3 mm) continuum observations of a selection of 64 cores previously identified from AzTEC/ASTE data (1.1 mm), along with previously known Class II BDs in the Lupus 1 and 3 molecular clouds. Surveyed archival data in the optical were used to complement these observations. We expect these ALMA observations prove efficient in detecting the youngest sources in these regions, since they probe the frequency domain at which these sources emit most of their radiation. We detected 19 sources from 15 ALMA fields. Considering all the pointings in our observing setup, the ALMA detection rate was ∼23% and the derived masses of the detected sources were between ∼0.18 and 124 M_{Jup}. We classified these sources according to their spectral energy distribution as 5 Class II sources, 2 new Class I/0 candidats, and 12 new possible pre-BD or deeply embedded protostellar candidates. We detected a promising candidate for a Class 0/I proto-BD source and inferred the disk dust mass of a bona fide Class II BD. The pre-BD cores might be the byproduct of an ongoing process of large-scale collapse. The Class II BD disks follow the correlation between disk mass and the mass of the central object that is observed at the low-mass stellar regime. We conclude that it is highly probable that the sources in the sample are formed as a scaled-down version of low-mass star formation, although disk fragmentation may be responsible for a considerable fraction of BDs

- Lupus1,3の分子雲に対しAzTEC/ASTE data (1.1mm)で同定されたコア64個をALMAでサーベイ
- 19個をALMAで検出．クラス分け
- Class II BDに関しては，中心星質量と円盤質量の相関を確認．BD形成はlow mass star formation のスケールダウンバージョンらしい

20.

Distinguishing between different mechanisms of FU-Orionis-type luminosity outbursts

Eduard I. Vorobyov, Vardan G. Elbakyan, Hauyu Baobab Liu, Michihiro Takami Aims. Accretion and luminosity bursts triggered by three distinct mechanisms: the magnetorotational instability in the inner disk regions, clump infall in gravitationally fragmented disks and close encounters with an intruder star, were studied to determine the disk kinematic characteristics that can help to distinguish between these burst mechanisms. Methods. Numerical hydrodynamics simulations in the thin-disk limit were employed to model the bursts in disk environments that are expected for each burst mechanism. Results. We found that the circumstellar disks featuring accretion bursts can bear kinematic features that are distinct for different burst mechanisms, which can be useful when identifying the burst origin. The disks in the stellar encounter and clump-infall models are characterized by tens of percent deviations from the Keplerian rotation, whie the disks in the MRI models are characterized only a few percent deviation, which is mostly caused by the gravitational instability that fuels the MRI bursts. Velocity channel maps also show distinct kinks and wiggles, which are caused by gas disk flows that are peculiar to each considered burst mechanism. The deviations of velocity channels in the burst-hosting disks from a symmetric pattern typical of Keplerian disks are strongest for the clump-infall and collision models, and carry individual features that may be useful for the identification of the corresponding burst mechanism. The considered burst mechanisms produce a variety of light curves with the burst amplitudes varying in the Δ m=2.5-3.7 limits, except for the clump-infall model where Δ m can reach 5.4, although the derived numbers may be affected by a small sample and boundary conditions. Conclusions. Burst triggering mechanisms are associated with distinct kinematic features in the burst-hosting disks that may be used for their identification. Abridged.

- FU Ori型星のメカニズムを区別する方法をシミュレーションをもとに考察
- アクリーションバーストの場合は，他のメカニズムでは見られないkinematical featuresを示すはず

21.

HII regions and high-mass starless clump candidates II. Fragmentation and induced star formation at 0.025 pc scale: An ALMA continuum study

S. Zhang, A. Zavagno, A. López-Sepulcre, H. Liu, F. Louvet, M. Figueira, D. Russeil, Y. Wu, J. Yuan, T. G. S. Pillai

The ionization feedback from HII regions modifies the properties of high-mass starless clumps (HMSCs, of several hundred to a few thousand solar masses with a size of 0.1-1 pc), such as temperature and turbulence, on the clump scale. The question of whether the presence of HII regions modifies the core-scale fragmentation and star formation in HMSCs remains to be explored. We aim to investigate the difference of 0.025 pc-scale fragmentation between candidate HMSCs that are strongly impacted by HII regions and less disturbed ones. We also search for evidence of mass shaping and induced star formation in the impacted HMSCs. Using the ALMA 1.3 mm continuum with a resolution of 1.3", we imaged eight candidate HMSCs, including four impacted by HII regions and another four situated in the quiet environment. The less-impacted HMSCs are selected on the basis of their similar mass and distance compared to the impacted ones to avoid any possible bias linked to these parameters. A total of 51 cores were detected in eight clumps, with three to nine cores for each clump. Within our limited sample, we did not find a clear difference in the 0.025 pc-scale fragmentation between impacted and non-impacted HMSCs, even though HII regions seem to affect the spatial distribution of the fragmented cores. Both types of HMSCs present a thermal fragmentation with two-level hierarchical features at the clump thermal Jeans length $\lambda^{th}_{J,clump}$ and $0.3\lambda^{th}_{J,clump}$. The ALMA emission morphology of the impacted HMSCs AGAL010.214-00.306 and AGAL018.931-00.029 sheds light on the capacities of HII regions to shape gas and dust in their surroundings and possibly to trigger star formation at 0.025 pc-scale in HMSCs. Future ALMA surveys covering a large number of impacted HMSCs with high turbulence are needed to confirm the trend of fragmentation indicated in this study.

- High Mass Starless Clumps (HMSCs)がHII領域から与えられるフィードバックの影響を調査
- ALMA 1.3mm連続波イメージにより，8つのHMSCsの構造調査，4つはHII領域の影響大のもの
- 内部に0.025pcのコアを計51個同定，HII領域の影響有無は見出せるほど明瞭な違いを生んでいなかった